nature communications

Article

https://doi.org/10.1038/s41467-026-73733-6

Protracted ocean circulation slowdown drove exceptional ice-sheet melting during ice age termination IV

Received: 26 July 2024

Accepted: 18 May 2026

Published online: 16 June 2026

Check for updates

Hsun-Ming Hu[1,2] ✉, Gianluca Marino[3] ✉, María Fernanda Sánchez Goñi[4], Eelco Rohling[5,6], Teresa Rodrigues[7,8], Carlos Pérez-Mejías[9], Qiuping Ren[10], Xiuyang Jiang[11], Véronique Michel[12,13], Patricia Valensi[14], Elisabetta Starnini[15], Marta Zunino[16], J. Sakari Salonen[4,17], Chieh-Ju Hsieh[2], Liangcheng Tan[1,9], Baptiste Chaigneau[4], Maud Chevalier[4] & Chuan-Chou Shen[2] ✉

Glacial terminations stand out for their high rates of sea-level rise, particularly during meltwater pulses. Termination IV (T-IV; ~340,000 years before present) is a prominent example, with sea level rising at up to ~5 m per century. Due to sparse absolute age constraints on marine records, the causes for the high rates of sea-level rise at T-IV remain elusive. In this work, we provide a speleothem chronology from northern Italy, which we transpose to North Atlantic marine records. We infer that the high T-IV sea-level rise rate likely relates to a feedback whereby protracted meltwater release caused enhanced ocean heat storage, followed by heat release upon circulation recovery, driving additional ice-sheet collapse. This analysis highlights the critical role of oceanic feedbacks in driving exceptional rates of sea-level rise during terminations.

Middle to Late Pleistocene climate records feature sharp transitions between maximum glacial and interglacial climate conditions, referred to as glacial terminations[1–3]. Terminations were first identified in benthic foraminiferal stable oxygen isotope ($\delta^{18}O_b$) records from deep-ocean sediment cores[4,5], where negative $\delta^{18}O_b$ shifts were ascribed to ice-volume reduction and associated release of ^{18}O-depleted meltwater to the ocean[6,7]. Independent sea-level reconstructions[8–11] have corroborated this picture and provided quantitative insights, showing strong agreement with individual and stacked benthic $\delta^{18}O_b$ time series that reflect both deep-ocean temperature and ice volume changes[12,13]. Detailed inspection of terminations reveals that ice-sheet retreat is not gradual; instead, there were times of accelerated collapse that led to meltwater pulses and remarkably high rates of sea-level rise[10,14]. Glacial terminations are also punctuated by millennial-scale climate perturbations, with abrupt shifts in oceanic and atmospheric temperatures and ocean circulation[15,16] that likely reflect bi-stability of the Atlantic

[1]State Key Laboratory of Loess Science, Institute of Earth Environment, Chinese Academy of Sciences, http://www.ieexa.cas.cn. [2]High-Precision Mass Spectrometry and Environment Change Laboratory (HISPEC), Department of Geosciences, National Taiwan University, http://www.gl.ntu.edu.tw. [3]Centro de Investigación Mariña, GEOMA, Palaeoclimatology Lab, Universidade de Vigo, Vigo, Spain. [4]Environnements et paléoenvironnements océaniques et continentaux (EPOC, UMR 5805), Univ. Bordeaux, CNRS, Bordeaux INP, EPHE, PSL University, Pessac, France. [5]Department of Earth Sciences, Utrecht University, Utrecht, The Netherlands. [6]Ocean and Earth Science, University of Southampton, National Oceanography Centre, Southampton, UK. [7]Portuguese Institute for Sea and Atmosphere (IPMA), Lisboa, Portugal. [8]Centro de Ciências do Mar do Algarve (CCMAR/CIMAR LA), Campus de Gambelas, Universidade do Algarve, Faro, Portugal. [9]Institute of Global Environmental Change, Xi'an Jiaotong University, https://hsce-en.xjtu.edu.cn. [10]CAS Key Laboratory of Ocean Circulation and Waves, Institute of Oceanology, Chinese Academy of Sciences, http://www.qdio.cas.cn. [11]Key Laboratory for Humid Subtropical Eco-Geographical Processes of the Ministry of Education, School of Geographical Sciences, Fujian Normal University, https://geo.fjnu.edu.cn/main.htm. [12]CNRS, CEPAM, Université Côte d'Azur, Nice, France. [13]Observatoire de la Côte d'Azur, CNRS, IRD, Géoazur, Université Côte d'Azur, Valbonne, France. [14]Laboratoire de Préhistoire Nice Côte d'Azur, Fondation IPH, UMR 7194 HNHP, Nice, France. [15]Department of Civilisation and Forms of Knowledge, University of Pisa, Pisa, Italy. [16]Toirano Cave, Toirano, Italy. [17]Department of Geosciences and Geography, University of Helsinki, Helsinki, Finland. ✉e-mail: hsunming.hu@gmail.com; gianluca.marino@uvigo.es; river@ntu.edu.tw

 https://doi.org/10.1038/s41467-026-73733-6

Meridional Overturning Circulation (AMOC)[17] during transitions between full glacial and interglacial climate states[18]. However, the relationships between ice-sheet collapse leading to meltwater pulses and AMOC slowdown remain elusive, even though their understanding is essential for an improved appreciation of interactions between the cryosphere and the ocean as key components of the deglaciation process[19–21].

A radiometrically constrained record of relative sea-level change reveals significant differences in the rates of sea-level rise between terminations[10]. Of particular interest is the meltwater pulse of Termination IV (T-IV, ~340 thousand years before present [kyr BP]) that featured rates of 49 ± 8 m kyr^{-1} (95% confidence bounds), higher than at any time over the past half a million years[10]. The underlying mechanisms responsible for the high rates of sea-level rise at terminations remain debated. Previous work indicates that the amount of continental ice accumulated during the preceding glacial period is an important factor, and that rapid sea-level rise events are often preceded by extended periods of ice melting[10]. Ice-sheet model simulations indicate that separation of the North American ice caps and subsequent collapse of the intervening ice saddle could have contributed to rapid sea-level rise[22,23], although the climatic context and relevance to the main meltwater pulse of the last termination remain debated[24]. Transient simulations with a general circulation model for the last two terminations indicate that subsurface warming across the Atlantic Ocean associated with AMOC slowdowns controls the overall melting rate of the ice accumulated during the preceding glacial maximum[25]. These studies have provided essential foundations and hypotheses, but the causes for the extreme rates of sea-level rise at most terminations remain elusive because of a dearth of quantitative proxy evidence and/or radiometrically constrained chronologies. This uncertainty underscores the need for quantitative proxy records with robust absolute chronologies to resolve not only the magnitudes and rates of sea-level rise but also the timing and duration of contemporaneous ocean and climate variations across different terminations, each shaped by distinct insolation and boundary conditions.

In this work we present radiometrically dated speleothem records from Bàsura cave in northern Italy ('Methods'; Supplementary Fig. 1). Stable carbon (δ^{13}C) and oxygen (δ^{18}O) isotopes ('Methods'; Supplementary Data 1) and trace element ratios (Sr/Ca; 'Methods'; Supplementary Data 2) were measured in flowstone cores BA2 and BA5-1 (Supplementary Fig. 2). The records span the ~380 to ~310 kyr BP interval, according to a chronology based on 30 ^{230}Th ages and the StalAge algorithm[26] ('Methods'; Supplementary Fig. 2; Supplementary Data 3). The sensitivity of these speleothem proxy records to hydroclimate changes in the North Atlantic region[27–31] underlies the synchronisation of records and transfer of the chronological constraints to North Atlantic palaeoclimate archives. For this, we chose the eastern North Atlantic Integrated Ocean Drilling Program (IODP) Site U1385 ('Methods'; Supplementary Fig. 1), from which we focus on the pollen data[32] ('Methods'; Supplementary Data 4) and the improved, higher resolution alkenone-based sea surface temperature (SST) reconstructions[33] ('Methods'; Supplementary Data 5). Our approach allows transferring a precise, radiometric chronology from Bàsura cave to key marine palaeoclimate records from the North Atlantic, thereby providing a chronological framework that is independent of orbital tuning and direct alignment to ice-core chronologies. We use this comprehensive dataset on its radiometrically constrained chronology and the output of fully coupled model simulations to decipher interactions between ice-sheet, oceanic, and climatic changes in the wider North Atlantic at orbital and millennial timescales during the fourth-last glacial-interglacial transition, which featured exceptionally high rates of sea-level rise[10].

Results and discussion

Chronological information, the time series of δ^{18}O and δ^{13}C ('Methods'; Supplementary Fig. 3), and Sr/Ca from Bàsura cave are shown in Fig. 1a–d. Our Bàsura cave chronology has relatively small uncertainties, notably across the 350–310 kyr BP interval, where they range between ±2.7 and ±0.3 kyr (2σ; Fig. 1a). The δ^{18}O time series (Fig. 1b) exhibits an abrupt increase at ~370 kyr BP, followed by a plateau, and then a gradual decrease beginning at ~358 kyr BP. A major negative excursion of ~2.8‰ occurs at 346–342 kyr BP, succeeded by a ~2‰ increase until 337 kyr BP, and then a second negative excursion of ~1.6‰ over the next ~2.5 kyr. From 334 to 329 kyr BP, Bàsura δ^{18}O increases by ~2.0‰ and then fluctuates until 310 kyr BP. The δ^{13}C record (Fig. 1c) shows a plateau of values around −11‰ from 380 to 370 kyr BP, which abruptly increases to −8‰ from 370 to 364 kyr BP. This is followed by a ~30-kyr-long interval of more positive values up to −5‰, which is punctuated by two prominent millennial-scale positive shifts at ~346 and ~334 kyr BP. Contemporaneous, positive peaks stand out also in the Sr/Ca time series, framing a long-term interval of consistently high Sr/Ca values. At ~334 kyr BP, both δ^{13}C and Sr/Ca shift abruptly towards more negative values, followed by broader, multi-millennial fluctuations in δ^{13}C lasting until 310 kyr BP.

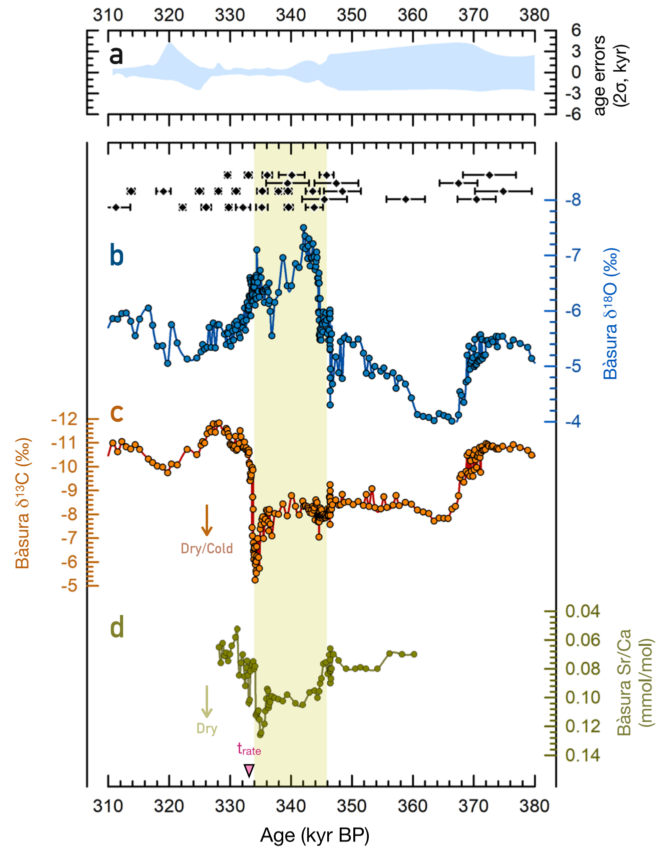

Fig. 1 | Speleothem BA2 from Bàsura cave, northern Italy. **a** Modelled age uncertainties of flowstone BA2, where blue shades indicate age uncertainties at the 2σ level. **b** Stable oxygen isotope (δ^{18}O) record. **c** Stable carbon isotope record (δ^{13}C). **d** Sr/Ca ratios. Yellowish-green bar indicates the period with positive δ^{13}C excursions. The black error bars on top of (**b**) indicate U-Th ages with 2σ errors. Pink triangle at the bottom indicates the timing of the sea-level rise rate maximum (t_{rate})[10].

Bàsura speleothem δ^{18}O primarily reflects precipitation δ^{18}O, which depends on both oceanic moisture source and rainfall amount effects[27]. During terminations, major moisture-source effects overshadow the δ^{18}O changes related to rainfall amount effects over the western Mediterranean[34]. Source effects are due to discharge of strongly ^{18}O-depleted meltwater into the North Atlantic from the collapse of circum-North Atlantic ice sheets[34,35], and into the Gulf of Genoa through the Rhône River from the deglaciation of Alpine glaciers[28] (Supplementary Fig. 1). The major negative δ^{18}O anomaly between ~346

https://doi.org/10.1038/s41467-026-73733-6

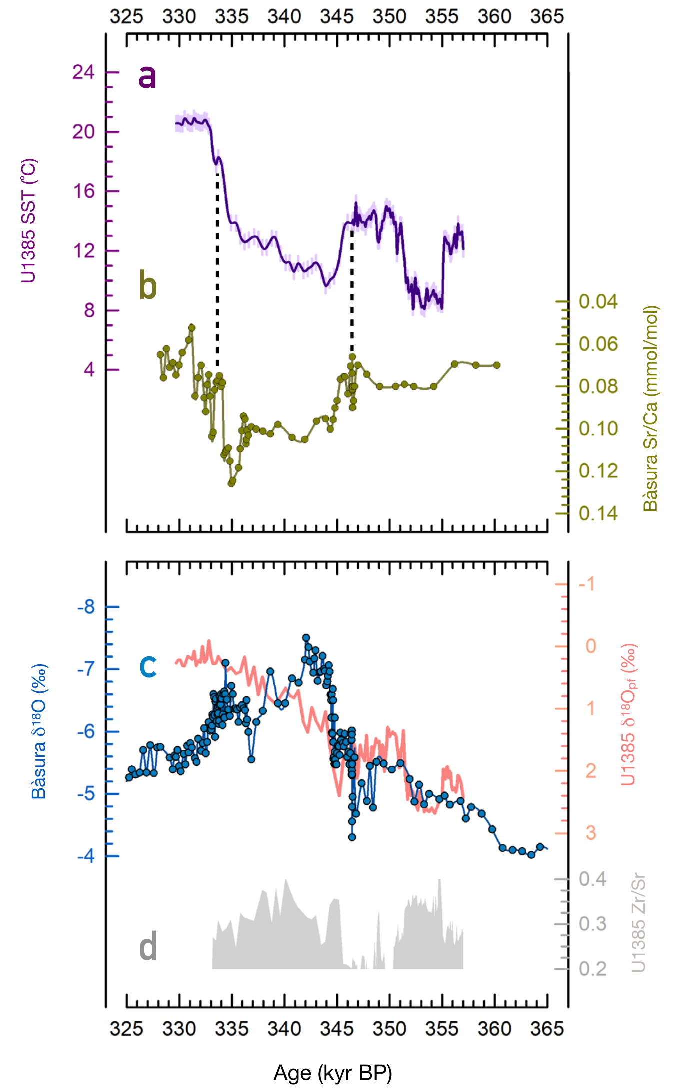

Fig. 2 | Synchronisation of the records from Integrated Ocean Drilling Program (IODP) Site U1385 to the Bàsura cave radiometric chronology. **a** Sea surface temperature (SST) record based on the alkenone unsaturation index ($U_{37}^{k'}$) from IODP Site U1385 on Bàsura chronology (this study). Light purple bars indicate 2σ uncertainty (±0.5 °C). **b** Bàsura Sr/Ca data. The dashed lines connecting (**a**, **b**) denote tie-points between Bàsura and Site U1385. **c** Bàsura $\delta^{18}O$ (circles) and planktonic foraminiferal $\delta^{18}O$ ($\delta^{18}O_{pf}$)[43] from Site U1385 (solid line) on Bàsura chronology (this study). **d** Zr/Sr ratios[16] of Site U1385 on Bàsura chronology (this study).

and ~334 kyr BP in Bàsura cave (Fig. 1b) most likely reflects such meltwater influences (Methods). The contemporaneous $\delta^{13}C$ increases (Fig. 1c) provide further insights into the nature of climate change across T-IV, in that they indicate prevailing cold and/or dry conditions like those observed during other terminations[36] and match simulations of the European climate response to terminal AMOC slowdowns[37]. High $\delta^{13}C$ relates to low soil bioactivity, long residence time in the karst systems, and increased prior calcite precipitation under cold and/or dry climates (Methods). Meltwater discharge from ice-sheet melting slows down the AMOC, leading to surface ocean and atmospheric cooling in the North Atlantic[37], which inhibits evaporation and reduces atmospheric moisture, leading to increased aridity along the southern European margin and the western Mediterranean region[38,39]. Within this context, the millennial-scale $\delta^{13}C$ positive excursions at ~346 and ~334 kyr BP likely indicate even colder and/or drier (stadial) climates, as documented in the prominent positive Sr/Ca peaks (Fig. 1d). The latter reflect long karst water residence times under dry climate conditions[40,41] (Methods). The large amplitude, abrupt $\delta^{13}C$ and Sr/Ca drops at ~334 kyr BP in Bàsura cave (Fig. 1c, d) then indicate enhanced water availability and regional warming, denoting the onset of interglacial conditions of Marine Isotope Stage (MIS) 9e. A key feature of the reconstructions from Bàsura cave presented here is a ~12.5 kyr interval of cold and/or dry conditions between 346.5 ± 2.5 kyr BP (2σ) and 333.7 ± 0.5 kyr BP (2σ), resembling those of the Heinrich stadials that punctuate other glacial terminations in the western Mediterranean region[42].

Building upon the response of Bàsura $\delta^{13}C$ and Sr/Ca to the North Atlantic millennial-scale Heinrich-like stadial of T-IV and the abrupt transition to MIS 9e, our precise speleothem radiometric chronology is transferred to the palaeoceanographic records from IODP Site U1385 (Fig. 2). The onset of abrupt Bàsura Sr/Ca increase at 346.5 ± 2.5 kyr BP (2σ) is considered to coincide with the initial SST reduction at 47.35 corrected revised metre composite depth [crmcd] in Site U1385 (ref. 43; Fig. 2a, b), reflecting the impact of a meltwater release on the regional climate through AMOC slowdown, similar to other terminations at the same site[33]. The abrupt negative Bàsura cave Sr/Ca shift at 333.7 ± 0.5 kyr BP (2σ) corresponds to the SST rise at 46.75 crmcd at Site U1385 (ref. 43) (Fig. 2a, b), interpreted as marking the end of T-IV and the transition to the interglacial climate of MIS 9e. This radiometrically constrained chronology for IODP Site U1385 (Methods) places at ~345 kyr BP an abrupt decrease in Site U1385 planktic foraminiferal $\delta^{18}O$ ($\delta^{18}O_{pf}$) that coincides with a large negative shift in Bàsura $\delta^{18}O$ (Fig. 2c) and with an abrupt increase in Zr/Sr also at Site U1385 (Fig. 2d), which reflects the local environmental response (detrital versus biogenic sedimentation) to Heinrich-like stadials at the Iberian Margin[16]. Cold and dry stadial conditions in the eastern North Atlantic and Mediterranean regions coincide with enhanced deglacial meltwater input to the ocean, causing lighter $\delta^{18}O_{pf}$ at Site U1385 and a contemporaneous decrease in speleothem $\delta^{18}O$ at Bàsura cave due to the above-mentioned source effect[34]. The ~1.4‰ negative $\delta^{18}O_{pf}$ shift at Site U1385 accounts for only ~50% of the ~2.8‰ change observed in speleothem $\delta^{18}O$ at this time, implying additional contribution from either SST cooling on $\delta^{18}O_{pf}$ or evaporation and reprecipitation at Bàsura cave from an ^{18}O-depleted seawater source. Meltwater input via the Rhône River from Alpine deglaciation into the Gulf of Genoa, a key site of Mediterranean cyclogenesis[28], may represent such a source (Methods). Our Bàsura cave to Site U1385 synchronisation is further and independently supported by concurrent increases in semi-desert pollen percentages (from 20 to 60%) at Site U1385 (Methods) and $\delta^{13}C$ (from −9 to −5‰) at Bàsura cave during 346–334 kyr BP (Fig. 3a), both indicating reduced regional precipitation.

Timing of T-IV and its Heinrich-like stadial

Heinrich-like stadials are a ubiquitous and distinctive feature of glacial terminations[18]. Our chronology based on Bàsura cave radiometrically constrains the timing and duration of T-IV and its associated Heinrich-like stadial, which was previously reported as HS10.1 (ref. 43). HS10.1 initiated with prominent (~5 °C) SST cooling at Site U1385, which began at 346.5 ± 2.5 kyr BP (Fig. 3b and Supplementary Fig. 4) and persisted until 334 ± 2.6 kyr BP. This cold interval is also documented by elevated $C_{37:4}$ percentages[44] at the same location (Fig. 3b). The end of this Heinrich-like stadial marks the transition to the MIS 9e interglacial, characterised by warmer SST and much lower semi-desert pollen percentages (~4%) at the Iberian Margin, together with a shift to more negative $\delta^{13}C$ at Bàsura cave (Fig. 3a, b) and winter atmospheric warming of ~10 °C (Supplementary Fig. 4). The timing of Heinrich-like conditions in the North Atlantic is broadly coeval with, or slightly outlasts, a weak phase of the Asian Monsoon[2] and reduced tropical rainfall in Borneo[45] (Fig. 3c). This phasing reflects the high to low-latitude climate response to the AMOC weakening during T-IV, superimposed upon the influence of orbital forcing on tropical

https://doi.org/10.1038/s41467-026-73733-6

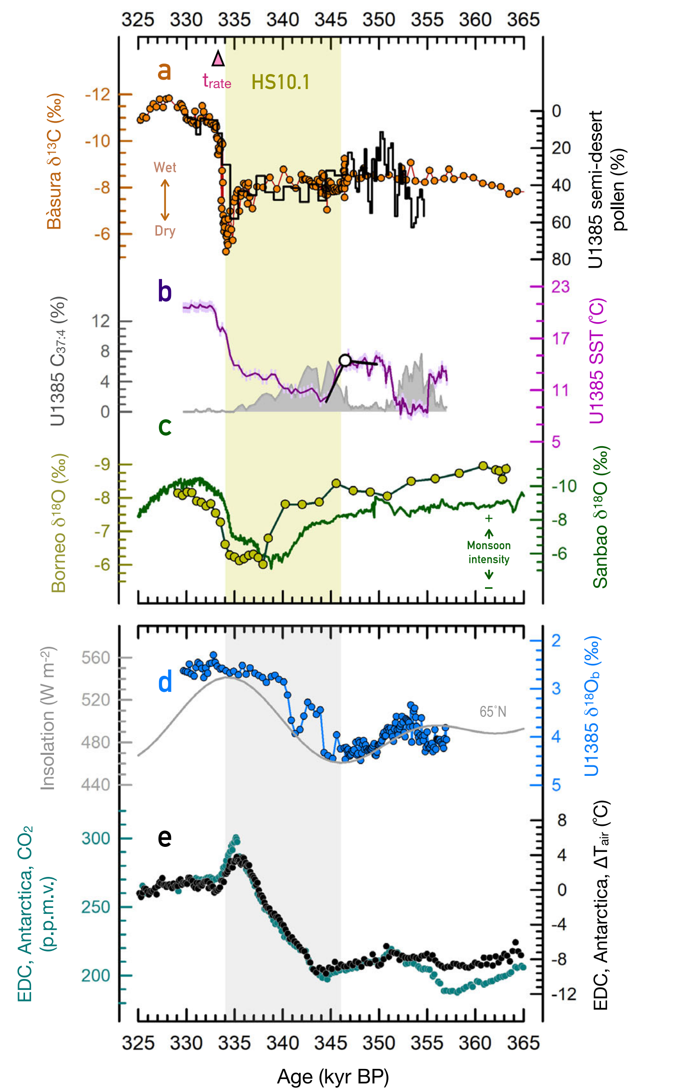

Fig. 3 | North Atlantic and Antarctic climate evolution during glacial termination IV. a Semi-desert pollen percentages in Site U1385 (black) on the radiometrically constrained chronology (this study) and Bàsura cave $\delta^{13}C$ (dark orange). **b** Site U1385 alkenone-based sea surface temperature (SST; dark purple; this study) and $C_{37:4}$ percentage (grey)[16] on the radiometrically constrained chronology (this study). High $C_{37:4}$ values denote cold conditions[44]. Light purple bars indicate 1σ uncertainty of SST (±0.5 °C). Black line and white open circle denote BREAKFIT change point analysis of U1385 SST time series. **c** Green: Chinese stalagmite $\delta^{18}O$ from Sanbao cave[1], where heavy values indicate weak Asian monsoon intensity. Yellow: Stalagmite $\delta^{18}O$ from Borneo[45], where heavy values indicate reduced precipitation. **d** Blue: Site U1385 benthic $\delta^{18}O$ ($\delta^{18}O_b$) on the radiometrically constrained chronology (this study). Grey: 21st June insolation changes at 65°N. **e** Atmospheric CO_2 concentrations[43] (parts per million by volume [p.p.m.v.]; black) and Antarctica air temperature anomaly[55] (ΔT_{air}; purple) from EPICA Dome C (EDC) on AICC2012 timescales[157]. Yellowish-green and greyish bars in (**a**, **c**) and (**d**, **e**), respectively, denote the periods of Heinrich-like stadial (HS) 10.1. Pink triangle at the top indicates the timing of the sea-level rise rate maximum (t_{rate})[10].

hydroclimate[45–47]. The pattern is consistent with observations from other terminations[1–3], including a southward shift of the Intertropical Convergence Zone[45,48], weakening of the Asian Monsoon[2,47], and drier conditions in the boreal tropics[45,46,49].

Inspection of the $\delta^{18}O_b$ allows placing millennial-scale events in the context of the underlying glacial-interglacial transition of T-IV, with the onset of the termination conventionally defined by the initial decrease in $\delta^{18}O_b$ (refs. 4,5). At Site U1385, this $\delta^{18}O_b$ change occurs at 345.2 ± 2.6 kyr BP (Fig. 3d; Supplementary Data 6) and coincides within uncertainties with the onset of the $\delta^{18}O_b$ negative shift at 342.2 ± 4.1 kyr BP in a recently published North Atlantic $\delta^{18}O_b$ stack[7]. Our radiometrically constrained chronology for Site U1385 thus lends independent support to that of the North Atlantic $\delta^{18}O_b$ stack, which relies on the synchronisation of North Atlantic ice-rafted debris (IRD) records with speleothems from distant Chinese caves[47]. These chronologies place the onset of T-IV several thousand years later than estimates based either on Menorcan speleothems[50] or on $^{40}Ar/^{39}Ar$-dated tephra layers in the aggradational successions of the sea-level-sensitive Paleotiber Delta[51]. Notably, the onset of the $\delta^{18}O_b$ decline at Site U1385 coincides with the initial rise in summer insolation at 65°N (Fig. 3d)[52], helping to resolve the long-standing debate on the previously reported lag of insolation behind $\delta^{18}O_b$ (ref. 53) that made T-IV anomalous among glacial terminations and seemingly inconsistent with the Milankovitch theory[54].

Records of Bàsura cave and Site U1385 (Fig. 3a, b) show that T-IV was marked by a prolonged cold/dry phase (Heinrich-like stadial) between 346.5 ± 2.5 and 334 ± 2.6 kyr BP, which spans the entire rising limb of boreal summer insolation[52] (Fig. 3d;). This sets T-IV apart from T-I[19], T-II[34], and T-III[36], where Heinrich-like stadials coincided with insolation increases but were less than 10 kyr in duration and did not encompass the full insolation rise. The exceptional duration of the Heinrich-like stadial of T-IV possibly reflects gradual ice-sheet melting under relatively weak orbital forcing at the onset of the termination, with boreal summer insolation increasing at low rates due to the combined effects of low (but rising) obliquity and maximum precession (Supplementary Fig. 5). Continuous meltwater discharge into the North Atlantic likely prolonged the Heinrich-like stadial relative to other terminations.

The exceptionally long duration of the Heinrich-like stadial of T-IV coincided with a major rise in atmospheric CO_2 concentrations[43] (~100 parts per million by volume [p.p.m.v.]; Fig. 3e) and a ~14°C rise in Antarctic temperature[55] (Fig. 3e). This interhemispheric coupling reflects the response of interhemispheric temperature[56] and atmospheric CO_2 concentrations[57] to Heinrich-like stadials. During these intervals, eddy-mediated heat transport facilitated the southward release of oceanic heat stored north of the Antarctic Circumpolar Current, driving Southern Ocean and Antarctic warming. The associated sea-ice retreat activated ice–albedo feedbacks, which further amplified regional warming[58,59].

Ocean, climate, and sea-level change during terminations

To investigate AMOC variability during T-IV, we constructed an AMOC index (Fig. 4a) using principal component analysis (PCA) in Bàsura $\delta^{13}C$, Sr/Ca, and U1385 SST records (Methods). These proxies are predominantly influenced by AMOC variability, and their combined signal captures the associated regional climate response[31,60,61]. The timing, magnitude, and rates of sea-level change during T-IV were assessed from the relative sea-level reconstruction obtained from the 'marginal sea method' applied to the Red Sea[10] (RSL_{Red}; Fig. 4b). Although RSL_{Red} underestimates global mean sea level (GMSL) by 8–20% at glacial maxima, its rate change (δ_{RSL}/δ_t) is indistinguishable from that of GMSL[10]. Because of its continuity, high resolution (~0.1 kyr), and a chronology tied to U-Th dated Chinese caves via Red Sea dust-speleothem $\delta^{18}O$ synchronisation[10], RSL_{Red} provides an ideal framework for comparison with our radiometrically constrained reconstruction of AMOC slowdown during T-IV.

Starting with the onset of the Heinrich-like stadial at 346.5 ± 2.5 kyr BP, the AMOC slowed down over a ~3 kyr interval (Fig. 4a), while RSL_{Red} remained broadly stable (Fig. 4b). At ~342 kyr BP, RSL_{Red} fell by ~10 m, followed by a ~30 m rise at modest rates (<10 m kyr^{-1}) through the remainder of the stadial until ~334 kyr BP. The AMOC subsequently resumed while δ_{RSL}/δ_t peaked at

49 ± 8 m kyr^{-1} (ref. 10; Fig. 4c), which coincided with the very latest stages of the cold and dry North Atlantic climate conditions that marked the protracted Heinrich-like stadial of T-IV. Chinese speleothem δ^{18}O (ref. 2) points to a similarity between T-IV and T-II, in that both (i) are one-step terminations, i.e. uninterrupted by millennial-scale warming (and strong AMOC[1]) episodes analogous to the Bølling–Allerød as for T-I; and (ii) coincide with high and rapidly rising boreal summer insolation forcing[1,19]. Data presented here point to a considerable difference between T-IV and T-II, in that the major T-II sea-level rise occurred during the Heinrich stadial within the termination[16], rather than at the end of it, as documented here for T-IV. The phasing between the Heinrich-like stadial and major sea-level rise during T-IV is more similar to T-I, when the major meltwater pulse (MWP-1A, ~14.7 kyr BP)[11,62,63] postdated Heinrich Stadial 1 (HS-1; 18–15 kyr BP)[64].

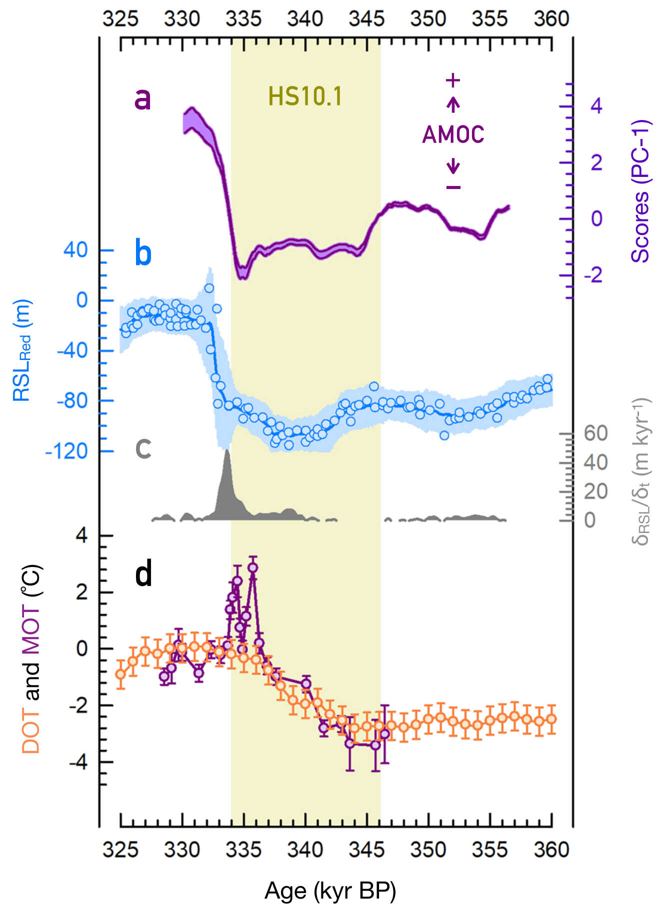

Fig. 4 | North Atlantic climate and sea-level changes. **a** Reconstructed Atlantic Meridional Overturning Circulation (AMOC) variability with associated 95% confidence limits (shaded envelopes) from Monte Carlo analysis of uncertainties in the relative principal component analysis and chronology (this study). **b** Relative sea-level reconstruction from the Red Sea (RSL_{Red})[10] with its 95% confidence level (light blue) and probability maximum of the model values (blue). **c** Rates of RSL_{Red} change (δ_{RSL}/δ_t)[10]. **d** Deep ocean temperature (DOT) reconstruction[83] (brown) and mean ocean temperature (MOT) record[70] (cyan) based on AICC2012 age model[157] with their 2σ uncertainties (colour-coded vertical bars). Yellowish-green vertical shade indicates the period of Heinrich-like stadial 10.1.

Next, we radiometrically constrained the time span between the onset of AMOC slowdown associated with the terminal Heinrich-like stadial and the peak in the rates of sea-level rise at each of the last five terminations. The onset of AMOC slowdowns was detected by applying a change-point analysis (BREAKFIT) algorithm[65] to proxy records that either reconstruct an AMOC weakening or document a curtailment in the associated northward heat transport (i.e. SST cooling; 'Methods'). For T-I, we focused on the ^{231}Pa/^{230}Th tracer of AMOC strength[66], while for T-II to T-V, we focused on neodymium isotopic data and/or North Atlantic SST records (Methods). Maximum rates of sea-level rise were determined using GMSL[11] for T-I, and the RSL_{Red} record[10] for T-II to T-V, given that the RSL_{Red} record is not continuous through T-I due to the presence of an aplanktonic interval during the last glacial maximum and the onset of T-I (refs. 10,67,68; 'Methods'). The time span between the onset of the AMOC slowdown and the peak rates of sea-level rise at each termination was calculated from the difference between their estimated ages (Table 1).

The probability density distributions of AMOC slowdown durations across T-I to T-V (Fig. 5a; Table 1) show that the AMOC slowdown of T-IV persisted for 12.9 kyr (10.2–15.6 kyr, 95% confidence bounds), outlasting any comparable event across the other terminations. Pearson correlation analysis, with uncertainties propagated using 1000 Monte Carlo realisations, *r*, reveals a strong coupling between AMOC slowdown durations and the magnitude of the peak rates of sea-level rise across the last five terminations (median r = 0.88; Fig. 5b). This relationship remains robust even when T-IV is excluded (median r = 0.77), demonstrating that the correlation is supported by, but not solely dependent on, the exceptional rates of sea-level rise during T-IV. To obtain independent radiometrically constrained estimates of sea-level change rates, we also computed the rates of change in the North Atlantic $\delta^{18}O_b$ stack[7] (Methods), given that $\delta^{18}O_b$ decreases during terminations partly reflects accelerated ice-volume reductions[7]. Despite considerable uncertainties, Pearson correlation analysis between $\delta^{18}O_b$ rates of change and AMOC slowdown durations yields a correlation coefficient of −0.81 ($p < 0.1$; Supplementary Fig. 6), consistent with our finding that the magnitude of the peak rates of sea-level rise is linked to the duration of AMOC slowdown. Taken together, these results suggest that the exceptionally prolonged AMOC slowdown during T-IV likely contributed to accelerated ice-sheet melting towards the end of the termination.

Table 1 | Data for the sea-level rate maximum and the duration of the AMOC slowdowns preceding sea level rate maximum over the last five terminations

Terminations	t_{AMOC} (kyr BP)[a]	t_{rate} (kyr BP)[b]	Durations (kyr)	Oceanic energy (× 10^{24}J)	Max δ_{SL}/δ_t (m kyr^{-1})[c]
T-I	18.1 ± 1.0	14.1 ± 1.0	4.0 ± 1.4	6.8 ± 3.9	25.4 ± 1.5
T-II	135.5 ± 1.2	132.6 ± 0.7	2.9 ± 1.4	5.2 ± 3.9	26.0 ± 7.7
T-III	250.1 ± 4.0	241.3 ± 0.5	8.8 ± 4.0	10.0 ± 3.9	37.4 ± 7.3
T-IV	346.5 ± 2.5	333.6 ± 0.6	12.9 ± 2.7	14.2 ± 3.9	48.5 ± 8.4
T-V	433.5 ± 4.0	428.8 ± 3.8	4.7 ± 5.5	3.8 ± 3.9	22.0 ± 7.8

All the errors are reported in 2σ.
[a]t_{AMOC}: onset timing of AMOC slowdowns.
[b]t_{rate}: timing of sea-level change rate maximum based on Lambeck et al.[11] (T-I) and Grant et al.[10] (T-II to T-V).
[c]Estimated sea-level change rate (δ_{SL}/δ_t) maximum[10,11].

https://doi.org/10.1038/s41467-026-73733-6

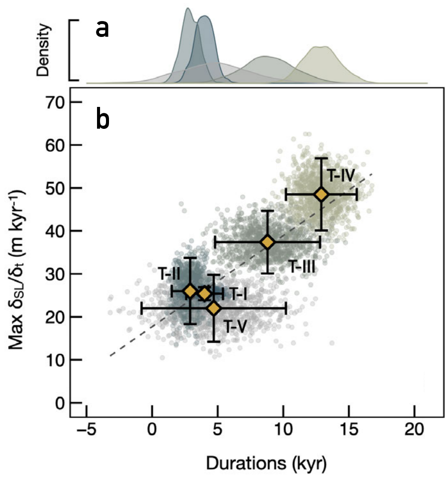

Fig. 5 | Slowdown of the Atlantic Meridional Overturning Circulation (AMOC) versus rates of sea-level rise. a Scatter density distribution of AMOC slowdown durations derived from 5000 Monte Carlo simulations for Terminations I–V (1000 simulations for each termination). The probability density analysis yields the following durations (with 95% confidence intervals). T-I: 4.0 kyr (2.6–5.4 kyr); T-II: 2.9 kyr (1.5–4.3 kyr); T-III: 8.8 kyr (4.8–12.8 kyr); T-IV: 12.9 kyr (10.2–15.6 kyr); T-V: 4.7 kyr (−0.8–10.2 kyr). **b** Correlation between the maximum rates of sea-level rise and the duration of AMOC slowdowns for Terminations I–V. **c** Correlation between the maximum rates of sea-level rise and the oceanic accumulated energy for Terminations I–V. Each scattered point in (**b**, **c**) represents an individual Monte Carlo realisation, while the diamond symbols denote the original estimates for each termination with error bars indicating 2σ uncertainties. The dashed lines in (**b**, **c**) show the best-fit linear regression.

Mechanisms of accelerated ice-sheet melting

Glacial terminations are associated with enhanced ocean heat content[69,70] (OHC), which we propose played a central role in accelerating ice-sheet melting and driving the associated sea-level rise (meltwater pulses). The iTraCE simulations[71] of the 11–20 kyr BP interval demonstrate a robust coupling between AMOC weakening and increased OHC (Methods), with longer slowdowns producing larger OHC anomalies. For example, a modelled ~3 kyr slowdown (18–15 kyr BP) generated an OHC anomaly of ~45 GJ m^{-2}, compared to ~40 GJ m^{-2} during a shorter ~1.3 kyr slowdown (13–11.7 kyr BP; Supplementary Fig. 7). A weakened AMOC stratifies the water column and suppresses convective ocean–atmosphere heat exchange, thereby trapping heat in the ocean interior[72–77]. Analysis of 19 CMIP6 models[78] forced with historical and future climate scenarios (SSP1-2.6, SSP2-4.5, SSP5-8.5; 'Methods') further supports the causal link between AMOC strength and basin-integrated OHC. Across the CMIP6 models, these variables are strongly and inversely correlated ($r = -0.73$, $p < 0.05$; Supplementary Fig. 8), indicating that this mechanism operates consistently across timescales and boundary conditions.

Building on these findings, we quantified heat storage in the ocean interior across the last five glacial terminations, using ice-core-based noble-gas reconstructions of mean ocean temperature (MOT)[69,70,79–81] and $\delta^{18}O_b$-based deep-ocean temperature (DOT) changes[82,83] (Methods). MOT variations provide a direct proxy for whole-ocean heat storage[80], whereas DOT reflects the integration of heat anomalies over long timescales[83] in the voluminous, slowly ventilated mid- to deep-ocean reservoir. These reconstructions indicate that the energy (heat) stored in the ocean interior scales with the peak rates of sea-level rise (Fig. 5c; median $r = 0.88$), with T-IV standing out for its exceptionally high values. Specifically, energy uptake associated with Heinrich-like event 10.1 during T-IV is estimated at ~1.3×10^{25} J and ~3.2×10^{25} J from DOT (~2.5 °C warming; Fig. 4d) and MOT (~6°C warming; Fig. 4d) reconstructions, respectively. During AMOC slowdowns, the accumulation of subsurface heat likely contributed to ice-sheet instability[84] and basal melting[72]. Upon AMOC recovery, this excess heat was redistributed to the surface ocean and atmosphere[85], providing energy for both ice melting and atmospheric warming[85–87]. High-resolution MOT records[70] during the last four terminations (Fig. 4d; Supplementary Figs. 9e, 10e, 11e) further support this scenario, showing transient cooling of ~0.3–3 °C that generally coincides with the maximum rates of sea-level rise. At T-IV, transient MOT cooling was larger and more abrupt than in previous terminations[70], suggesting that heat released at the end of the Heinrich-like stadial drove the exceptionally high rates of sea-level rise observed at ~334 ka BP. The process is also consistent with model results[25,85] (Supplementary Fig. 12; 'Methods') that simulate subsurface heat buildup during AMOC weak phases, followed by surface-ocean warming and accelerated sea-level rise upon AMOC recovery.

High radiative forcing from rising atmospheric CO_2 and enhanced summer insolation at the end of T-IV likely contributed to major ice-sheet melting. Atmospheric CO_2 reached ~310 p.p.m.v. when the rates of sea-level rise peaked[43], which is the highest value among the last five terminations at their respective meltwater pulses (Supplementary Figs. 9f, 10d, 11d, 13e). This CO_2 rise (~100 p.p.m.v. relative to the preceding glacial maximum; Fig. 3e) produced an additional +2.2 W m^{-2} of radiative forcing[88], exceeding that associated with meltwater pulses at other terminations (T-I, T-II, T-III, and T-V), where CO_2 increases of 30–80 p.p.m.v. generated +0.8 to +1.8 W m^{-2} of radiative forcing. Similarly, caloric summer half-year insolation at 65°N reached 6.085 GJ m^{-2} at the end of T-IV (Supplementary Fig. 5), higher than during T-I (5.992 GJ m^{-2}), T-II (5.999 GJ m^{-2}), T-III (5.955 GJ m^{-2}), and T-V (5.817 GJ m^{-2}). The combined effects of elevated CO_2 concentrations and enhanced summer insolation likely maximised the rates of sea-level rise at the end of T-IV by amplifying surface melting through multiple feedbacks, including albedo-driven absorption of solar radiation[89], hydrofracturing and the consequent loss of buttressing[90,91], and circulation-induced expansion of ablation zones[92].

Although our analysis provides a quantitative assessment of the relationship between oceanic heat storage and magnitude of meltwater pulses during the past five glacial terminations, uncertainties remain. These include the source and volume of meltwater and potential modulation by ice-sheet geometry and grounding-line configuration[22,23]. Reconstructions for intervals older than T-I remain too sparse to quantitatively address these factors. For T-IV, ice-volume reconstructions (Supplementary Fig. 14; 'Methods')[83,93] suggest that Northern Hemisphere ice sheets supplied ~80–90% of meltwater, with Antarctica contributing ~10–20%, while the exact magnitude remains difficult to quantify.

 https://doi.org/10.1038/s41467-026-73733-6

Our analysis suggests that abrupt release of the heat stored in the ocean interior during the multimillennial-scale episodes of AMOC weakening at glacial terminations primed the ocean–atmosphere–cryosphere system for rapid ice-sheet collapse and attendant high rates of sea-level rise, with T-IV representing an extreme manifestation of this mechanism. Radiative forcing from high atmospheric CO_2 concentrations and enhanced boreal summer insolation likely acted alongside oceanic heat to maximise ice-sheet melting. Our study therefore underscores the broader climatic risk posed by AMOC weakening, an increasingly recognised feature of the Earth system[94]. Future integrative efforts combining palaeoclimate constraints with fully coupled transient simulations will be essential to resolve how the heat stored in the ocean interior is transferred to the upper ocean and atmosphere, amplifies ice-sheet melt, and ultimately drives rapid sea-level rise.

Methods

Samples and isotope analyses

Flowstone cores BA2 and BA5-1 (Supplementary Fig. 2a, b) were collected from a chamber located 650 metres from Bàsura cave entrance. The speleothems were halved and carefully polished. Depth intervals of 260–336 mm from BA2 and 560–591 mm from BA5-1 were analysed in this study.

For stable oxygen ($\delta^{18}O$) and carbon ($\delta^{13}C$) isotope measurements, 194 subsamples from BA5-1 and 254 subsamples from BA2 were analysed, using Thermo-Finnigan MAT 253 and Micromass IsoPrime mass spectrometers at Fujian Normal University. All values are reported in per mil (‰) relative to the Vienna PeeDee Belemnite (VPDB) standard, using the NBS-19 ($\delta^{18}O = -2.20$‰, $\delta^{13}C = 1.95$‰) carbonate standard as the reference. Analytical reproducibility (1σ) was ±0.12‰ for $\delta^{18}O$ and ±0.06‰ for $\delta^{13}C$. The dataset is provided as Supplementary Data 1.

U-Th dating

For U-Th chemistry[95] and instrumental analysis[96,97], 10 subsamples and 20 subsamples of 0.3–4 g were taken from BA5-1 and BA2, respectively. These subsamples were analysed using a Thermo-Finnigan Neptune multi-collector inductively coupled plasma mass spectrometer. Decay constants used are 9.1705×10^{-6} yr^{-1} for ^{230}Th (ref. 97), 2.8215×10^{-6} yr^{-1} for ^{234}U (ref. 98), and 1.55125×10^{-10} yr^{-1} for ^{238}U (ref. 99). Uncertainties in the U-Th dates were calculated at the 2σ level, representing two standard deviations from the mean, unless otherwise stated. The depth-age model was established using the StalAge algorithm[26] (Supplementary Fig. 2c), which employs Monte Carlo simulations to estimate the median age and associated 95% confidence intervals at depths corresponding to measured proxy data. A detailed dating report following the U-series community data-reporting standards[100] is provided in Supplementary Data 2.

Trace element analyses

A total of 80 powdered subsamples (10–50 µg each) from BA2 were micro-milled at intervals of 0.2–1.0 mm along the growth axis. These subsamples were analysed for Sr/Ca ratios using a Thermo-Finnigan Element II inductively coupled plasma sector field mass spectrometer (ICP-SF-MS). External matrix-matched standards were analysed every five samples to ensure analytical accuracy, with 2σ reproducibility of ±0.5% (ref. 101). The data are available in Supplementary Data 3.

Pollen analysis

Seventy-three subsamples from Integrated Ocean Drilling Program (IODP) Site U1385, between 48.98 and 45.847 corrected revised metres composite depth (crmcd), were collected every 4 cm (~0.49 kyr average temporal resolution) for pollen identification and counting. Sediment subsamples, 1 cm in thickness and 1.5–3.5 cm^{-3} in volume, were prepared for pollen analysis using the standard protocol for marine samples[102]. This involves coarse-sieving (150 µm mesh), successive treatments with cold HCl, cold HF at increasing strength, and micro-sieving (10 µm mesh). Known quantities of *Lycopodium* spores in tablet form were added to permit calculation of pollen concentrations. Slides were prepared using a mobile mounting medium to permit rotation of the grains and counted using a Primo Star light microscope at 400× and 1000× magnifications for identification of pollen and spores.

Over ~100 pollen grains (100–133), excluding the *Pinus* dominant taxon in deep-sea sedimentary sequences[103], and 20 morphotypes were counted to obtain a reliable representation of the vegetation source[104,105] of Site U1385. The number of pollen morphotypes in 67 out of 73 samples ranges from 20 to 29, and from 17 to 19 morphotypes in the remaining samples. Pollen percentages for terrestrial taxa were calculated against the main sum of terrestrial grains, while percentages for *Pinus* were calculated against the main sum plus *Pinus*. Aquatic pollen and spore percentages are based on the total sum (Pollen + spores + indeterminables + unknowns). The average uncertainty of calculated pollen percentage values in our analysis is less than 8% (ref. 106). The pollen diagram (Supplementary Fig. 16) was drawn with the Psimpoll software[107] and a visual pollen zonation was defined based on percentage variations of at least two pollen taxa with different ecological affinities[108]. This visual interpretation is supported by hierarchical clustering analysis based on minimisation of the Euclidean distance and constrained by the number of sample depths using the package Rioja in R (ref. 109).

Sea surface temperature reconstruction

A total of 255 subsamples from Site U1385 were collected every 2 cm between 49.86 and 45.24 crmcd, corresponding to an average temporal resolution of ~290 years. Sediment subsamples of 1 cm in thickness and ~2.5 cm^3 in volume were prepared for alkenone analyses. Alkenones, heptatriaconta-8*E*,15*E*,22*E*-trien-2-one (tri-unsaturated) and heptatriaconta-15*E*,22*E*-dien-2-one (di-unsaturated), were extracted from sediments, purified using organic solvents, and quantified using a Varian 3800 gas chromatograph equipped with a septum programmable injector, a flame ionisation detector (FID), and a CPSIL-5 CB capillary column (coated with 100% dimethylsiloxane; film thickness: 0.12 µm; column dimensions: 50 m length × 0.32 mm inner diameter [ID] × 0.45 mm outer diameter [OD]; carrier gas: hydrogen at a flow rate of 2.5 mL min^{-1}). Alkenone concentrations were determined using *n*-hexatriacontane as an internal standard, with absolute concentration uncertainties below 10%. Sea surface temperature (SST) was reconstructed from the relative concentrations of di- and tri-unsaturated C_{37} alkenones using the calibration equation of Müller et al.[110]. Reproducibility tests showed that 1σ uncertainty in the alkenone-derived SST is ±0.5 °C (refs. 33,111).

Bàsura cave

Bàsura cave is situated in the coastal area of the Gulf of Genoa (44°08′N and 8°12′E; 200 m above sea level; Supplementary Fig. 1), in the Liguria region of northern Italy. The region features the typical Mediterranean climate, that is, mild and humid winters and hot and dry summers[27]. The cave developed within Triassic limestone of the Monte San Pietro formation (Briançon series), which also contains dolostones. Surrounding vegetation is dominated by grasslands (e.g. *Brachypodium ramosum*, *Tuberaria guttata*) and forests predominantly composed of *Pinus halepensis*. Patches of shrubland dominated by species of the family *Lamiaceae* and scattered olive groves (*Olea europaea*) occur throughout the area.

Integrated Ocean Drilling Program Site U1385

Integrated Ocean Drilling Program (IODP) Site U1385 (37°20′N, 10°04′ W, 2578 m water depth), also referred to as 'Shackleton site', was drilled in the southwestern Iberian margin during IODP Expedition 339 (Supplementary Fig. 1). The site is located on the Promontorio dos Principes de Avis, along the continental slope of the southwestern

Iberian margin, which is elevated above the abyssal plain and thus devoid of turbidites[112]. Today, Site U1385 is bathed by North Atlantic Deep Water, whereas during glacial periods, southern-sourced deep waters prevailed[113]. Due to its proximity to the Tagus River, Site U1385 receives a significant amount of continental material, including terrigenous material[16] and pollen grains[112].

The 150 m-long sedimentary section recovered at Site U1385 comprises hemipelagic sediments typical of continental margin settings that settled through a well-ventilated water column and accumulated at average rates of 10 cm kyr^{-1} (ref. 114). The existing stratigraphy of Site U1385 was built upon a combination of chemostratigraphic proxies[115].

Composite chronology for BA2 $\delta^{18}O$ and $\delta^{13}C$

Unlike the speleothem record of flowstone BA2, the record from flowstone BA5-1 does not span the full duration of glacial Termination IV (T-IV) but has a more precise chronology (Supplementary Fig. 2). To improve dating accuracy and reduce uncertainties of the chronology of BA2, we tuned the BA2 $\delta^{18}O$ record to that of BA5-1 through the 315–338 kyr BP interval, which is covered in both flowstone cores. A new age model for BA2 was then built using its original dating points along with 11 additional age-control points from BA5-1 (Supplementary Fig. 2c). The original stable isotope records and tuning results are shown in Supplementary Fig. 3. Tuning the BA2 record to BA5-1 using either $\delta^{18}O$ or $\delta^{13}C$ yielded consistent results.

Interpretation of Bàsura $\delta^{18}O$

Results of both $\delta^{18}O$ and $\delta^{13}C$ from BA5-1 and BA2 exhibit good agreement through the intervals where the two flowstones overlap (Supplementary Fig. 3), which suggests that speleothem carbonates were deposited in conditions of (or close to) isotopic equilibrium. Accordingly, the $\delta^{18}O$ or $\delta^{13}C$ records presented here from Bàsura cave reflect and allow reconstructing past environmental changes[116]. Bàsura $\delta^{18}O$ primarily reflects recharge-weighted drip water $\delta^{18}O$. This mostly derives from rainfall precipitation during late autumn to early spring, while the region experiences high evapotranspiration (50–70% of the annual precipitation) during the hot and dry summers[117].

Speleothem $\delta^{18}O$ at Bàsura cave is primarily governed by the source-water and amount effects, given that air temperature effects on rainfall $\delta^{18}O$ counterbalance temperature-dependent $\delta^{18}O$ fractionation during carbonate deposition[27]. The amount effect refers to the phenomenon where increased precipitation, coupled with strong Rayleigh fractionation, results in more negative $\delta^{18}O$ values in precipitation $\delta^{18}O$, and thus in lighter speleothem $\delta^{18}O$ (ref. 118). The source-water effect is manifested in Bàsura cave in two ways. Firstly, it involves shifts in the moisture source region, with Atlantic-sourced moisture (−8.5‰, ref. 119) contributing more negative $\delta^{18}O$ values than Mediterranean-sourced moisture (−4.6‰, ref. 119). Secondly, changes in seawater $\delta^{18}O$ due to the discharge of large volumes ^{18}O-depleted meltwater into the North Atlantic Ocean shift the seawater $\delta^{18}O$ towards more negative values during glacial terminations[34]. Changes in the $\delta^{18}O$ of the moisture source influence precipitation $\delta^{18}O$, hence speleothem $\delta^{18}O$ within the cave.

Interpretation of the Bàsura $\delta^{18}O$ between ~380 and ~310 kyr BP accounts for several processes that operated together, such as seasonal precipitation patterns, location of the moisture source(s), and timing of meltwater inputs from Northern Hemisphere ice sheets and Alpine glaciers. The processes could have weighted differently on local precipitation $\delta^{18}O$ under different orbital configurations, climate states (glacial, interglacial), and millennial-scale episodes of climate change (e.g. Heinrich-like stadials). However, the meltwater impacts on seawater $\delta^{18}O$ during T-IV were probably the dominant factor that controlled speleothem $\delta^{18}O$ at Bàsura cave. This source-water effect[34] has been used before to correlate marine sediments and speleothem records during other glacial terminations [35]. Although our synchronisation of marine records to speleothem chronologies does not rely on this approach, we noted that the ~2.8‰ decreases in Bàsura $\delta^{18}O$ coincided with a negative shift of ~1.7‰ in Site U1385 planktonic foraminiferal $\delta^{18}O$ ($\delta^{18}O_{pf}$, ref. 43, Supplementary Fig. 15a) and of ~2‰ in the $\delta^{18}O_{pf}$ of Mediterranean marine core KC01B (ref. 120, Supplementary Fig. 15b). Alpine glaciers, being smaller and located at lower latitudes than the major ice sheets[121] (Supplementary Fig. 1), could in principle predate deglaciation of major continental ice sheets, discharging meltwater directly into the northwestern Mediterranean Sea. Hence, the Bàsura $\delta^{18}O$ drop at 345.4 ± 1.6 kyr BP likely reflects a cumulative response to meltwater influences from both major ice sheets (into the North Atlantic Ocean) and Alpine glaciers (into the Mediterranean Sea).

Interpretation of Bàsura $\delta^{13}C$ and trace elements

Stalagmite $\delta^{13}C$ in Bàsura cave is influenced by various factors. The $\delta^{13}C$ of soil CO_2 is inherited from the atmosphere, and soil respiration plays a significant role[122,123]. Vegetation types and their photosynthetic pathways also affect $\delta^{13}C$ values, with C3 plants leading to a range of −6 to −14‰ and C4 plants to higher values, with a range of +2 to −6‰ (ref. 124). The observed $\delta^{13}C$ values in the cave agree with the dominant plants in the surrounding vegetation, which are of C3 type. Changes in vegetation unlikely control the $\delta^{13}C$ variations at Bàsura cave, as the region has been consistently dominated by C3 plants during both glacial and interglacial periods[125,126].

Under warm and humid conditions, dense vegetation cover and increased soil activity can lead to negative soil $\delta^{13}C$ (ref. 122). Increased precipitation enhances drip water rates and infiltration, reduces CO_2 degassing, and results in more negative speleothem $\delta^{13}C$ values[127,128]. Prior carbonate precipitation (PCP) before water drips into the cave[122] is another factor affecting $\delta^{13}C$. In dry conditions, long infiltration residence times favour PCP, which enriches both aqueous solution and stalagmite in ^{13}C. PCP is reduced in wet conditions with short infiltration residence times, leading to ^{13}C-depletion in the aqueous solution and stalagmite. In sum, warm and/or humid climates promote soil activity and vegetation cover, decrease PCP, and lower stalagmite $\delta^{13}C$, and vice versa. Similarly, drip water chemistry data[41] show that Sr/Ca ratios in Bàsura cave drip waters are affected by changes in modern rainfall, specifically indicating the occurrence of PCP. Dry climate increases the residence time of the infiltrated water in the epikarst and lowers the drip rates, which enhances CO_2 degassing and favours PCP. High Sr/Ca ratios during dry periods arise from preferential Ca removal due to PCP[129,130].

Radiometrically constrained chronology for IODP Site U1385

The chronology of Site U1385 used in this study is primarily based on synchronisation to the new radiometric chronology of Bàsura cave, derived from U-Th dated flowstones BA5-1 and BA2. The lowermost (49.45 corrected revised metre composite depth [crmcd]) and uppermost (46.37 crmcd) tie-points are taken from a recently published hybrid age model[16] of Site U1385 and have assigned ages of 357.0 ± 4.0 kyr BP and 329.7 ± 4.0 kyr BP, respectively. The two tie points that were obtained through synchronisation to Bàsura cave Sr/Ca (Fig. 2a, b) have assigned ages of 346.5 ± 2.5 kyr BP (tied 47.35 crmcd from Site U1385) and 333.7 ± 0.5 kyr BP (tied to 46.75 crmcd from Site U1385). The Bàsura age of 346.5 ± 2.5 kyr BP corresponds to the onset of an abrupt Sr/Ca increase, which marks the onset of the climate deterioration (towards colder and/or drier conditions) associated with the Heinrich-like stadial of T-IV. The prominent negative shift in Sr/Ca at 333.7 ± 0.5 kyr BP is tied to a concurrent rise in sea surface temperature (SST) at Site U1385, indicating the transition to interglacial conditions both on land and in the ocean (warmer and/or more humid climates).

We compared our new chronology with four existing chronologies[16] for Site U1385 across the relevant time span, including a

 https://doi.org/10.1038/s41467-026-73733-6

hybrid age model[16] that integrates chronological information from various archives, including ice cores and speleothems. Other age models for Site U1385 were built through correlation to global benthic $\delta^{18}O$ ($\delta^{18}O_b$) stack (LR04, ref. 6), to the probabilistic $\delta^{18}O_b$ stack (Prob-stack, ref. 131), and to the Mediterranean $\delta^{18}O_b$ (Med $\delta^{18}O_b$, ref. 132). For the topmost section, these chronologies yield ages of 329.71 (hybrid model), 327.12 (LR04), 327.47 (Prob-stack), and 329.71 kyr BP (Med $\delta^{18}O_b$). At the bottom of the section, ages from all four age models are identical, namely 356.99 (hybrid model), 356.98 (Lisiecki and Raymo), 356.99 (Ahn), and 356.99 kyr BP (Med $\delta^{18}O_b$). Thus, the choice of the chronology introduces a maximum age offset of 2.1 kyr in the topmost section, which does not affect the conclusions of our study.

The chronological uncertainties (2σ) at the top and bottom of the Site U1385 interval used in this study are from the hybrid age model of Hodell et al.[16]) and amount to ±4.0 and ±4.8 kyr, respectively. For the interval synchronised to the Bàsura cave's chronology, the propagated age uncertainties were calculated following the methodology of Marino et al.[34]). Specifically, we accounted for all relevant sources of uncertainty, including the: (i) radiometric chronology of Bàsura speleothems, which is based on U-Th dating and on the StalAge algorithm[26]; (ii) sample spacing (i.e. temporal resolution at the tie points) in the Bàsura Sr/Ca time series; and (iii) sample spacing of the SST record from Site U1385. These uncertainties were combined in a mean-squared estimate (MSE) at the 95% probability level. The radiometrically constrained chronology for the SST time series from Site U1385 with the associated uncertainties is available as Supplementary Data 6.

Pollen results and pollen-based climate reconstructions in IODP Site U1385

Pollen concentrations at Site U1385 range from 656 to 42,049 grains cm^{-3} in the sections that precede and cover T-IV and interglacial marine isotope stage (MIS) 9e. Cluster analysis reveals three major pollen zones in the percentage diagram, which delineate significant shifts in vegetation cover and composition along the southwestern Iberian margin (Supplementary Fig. 16). Pollen data covering the interval from ~342 to ~334 kyr BP were previously reported[32], while this study extends this record back in time to include the interval from ~356 to ~342 kyr BP.

Pollen zone 1 is characterised by high percentages of *Pinus*, pioneer trees and shrubs, and semi-desert taxa, all of which decrease towards the end of the zone. The data pattern suggests a climatic shift from cool and dry towards more humid conditions. The onset of pollen zone 2 is marked by elevated percentages of Ericaceae (~30%), followed by a near doubling of the semi-desert taxa and the increase of pioneer trees and shrubs. This is accompanied by persistently low percentages of Mediterranean forest taxa and a subsequent reduction in Ericaceae. Zone 2 corresponds temporally to the T-IV interval, which is defined by a pronounced increase in $\delta^{18}O_b$ values at Site U1385. The pollen assemblages reflect open vegetation conditions indicative of cold climatic conditions throughout T-IV, with the driest period coinciding with the lowest sea surface temperatures at the end of T-IV.

Pollen zone 3 is characterised by a significant (~40%) reduction in semi-desert pollen percentages, coinciding with increased Mediterranean forest and Ericaceae pollen from approximately 20 to 60% and from 10 to 30%, respectively. Previous studies indicate that pollen percentages of Mediterranean trees and shrubs exceeding 20% correspond to forested environments[133]. Therefore, pollen zone 3 marks the onset of interglacial (MIS 9e) conditions on land[134]. The development of the Mediterranean forest within this zone suggests enhanced atmospheric warming and moisture availability. This zone shows the highest abundance of sclerophyllous taxa, indicating pronounced seasonal contrasts that are typical of the modern Mediterranean climate[135] (wet and cool winters, hot and dry summers). The pollen assemblage in this zone includes a marked increase in *Isoetes* spores, which exhibit four times higher percentages than in pollen zone 2 at this location. Such an increase typically occurs during glacial terminations, as the marshland habitat preferred by *Isoetes* expands in response to higher precipitation during glacial-interglacial transitions[136]. A notable reduction in pollen concentrations occurs concurrently with the maximum expansion of Mediterranean forest taxa, likely resulting from abrupt sea-level rise (meltwater pulse) at the end of T-IV. This sea-level rise would have abruptly increased the distance between Site U1385 and nearby continental sources, thus reducing pollen input and providing additional evidence for substantial ice-sheet melting at this time. The final stage of pollen zone 3 documents a gradual reduction of Mediterranean forest, along with peak abundances of *Isoetes* spores and widespread generalist taxa. Climatic conditions during this interval remain relatively warm and humid, although a reduction in sclerophyllous taxa suggests weakened seasonality compared to the preceding interval, possibly indicating somewhat cooler and more uniformly moist conditions year-round.

We reconstructed December to February precipitation and temperature changes on land from the fossil pollen data using five pollen-climate calibration methods[137]: weighted averaging, weighted averaging-partial least squares, modern-analogue technique, random forest, and boosted regression tree. Correlation analysis between Bàsura $\delta^{13}C$ and the ensemble means of pollen-based temperature and precipitation derived from the five methods reveals significant correlation coefficients of −0.78 and −0.81 ($p < 0.05$) (Supplementary Fig. 4), lending independent support to our reconstructions based on Bàsura cave $\delta^{13}C$.

Principal component analysis

Principal component analysis (PCA) is a statistical method that reduces dimensionality in a multivariate dataset while retaining as much of the dataset's variance as possible[138]. PCA identifies new, mutually orthogonal axes (principal components) that capture variance in descending order when applied to correlated variables. The first principal component (PC1) explains the largest portion of the total variance, and subsequent principal components capture decreasing amounts of the remaining variance.

We applied PCA to three time series: (*1*) Bàsura cave Sr/Ca; (*2*) Bàsura cave $\delta^{13}C$; and (*3*) SST from IODP Site U1385. PC1 reflects the dominant pattern shared by the speleothem proxies and the Iberian Margin SST record, interpreted as the response of the regional climate to strength variations of the Atlantic Meridional Overturning Circulation (AMOC) during T-IV. Palaeoclimate evidence[31,139,140] indicates that a stronger AMOC enhances the: (i) moisture transport to the Mediterranean region, reflected as lower speleothem Sr/Ca and $\delta^{13}C$ at Bàsura cave in northern Italy; and (ii) northward heat transport in the Atlantic Ocean, resulting in higher SSTs at Iberian Margin Site U1385. Conversely, a weaker AMOC produces cooler, drier conditions in the Mediterranean (higher Sr/Ca and $\delta^{13}C$ values at Bàsura cave) and cooler SST at Site U1385. Our analysis indicates that PC1 explains 53% of $\delta^{13}C$ variance, 80% of Sr/Ca variance, and 65% of SST variance. We evaluated the confidence levels of PC1, by employing a Monte Carlo approach. For each proxy record, we randomly sampled each data point of the time series 1000 times within its age and proxy uncertainties. Each of these 1000 realisations was then linearly interpolated onto a common, equally spaced timescale. Next, we computed the 68% (16th–84th percentile) and 95% (2.5th–97.5th percentile) confidence intervals, as well as the probability maximum (modal value) for PC1. The 95% probability interval around this modal value provides a robust measure of the range of plausible PC1 probability maxima.

Variability of the Atlantic Meridional Overturning Circulation

The AMOC variability during T-IV is discussed in the main text, with additional insights into the approach we used to reconstruct this

https://doi.org/10.1038/s41467-026-73733-6

variability provided in 'Methods'. In the following, we expand on proxy evidence for AMOC strength variations across T-I, T-II, T-III, and T-V. We employ a multi-proxy approach that ensures a robust interpretation of AMOC changes, particularly in cases where single-proxy records may be influenced by factors other than the AMOC.

In the absence of the kinematic proxy for changes in the strength of the AMOC based on $^{231}Pa/^{230}Th$ ratios[66], North Atlantic SST variability serves as a proxy for AMOC changes when supported by additional evidence[141,142]. In addition to the AMOC variability, North Atlantic SST is influenced by a combination of factors, including atmospheric forcing (e.g. wind patterns, heat fluxes), freshwater inputs (e.g. ice-sheets, rivers), and precipitation changes that, in turn, modulate sea-surface salinity and temperature patterns[143–145]. Although non-AMOC factors can complicate the reconstruction of the AMOC strength based on North Atlantic SST proxy records, large-amplitude, abrupt AMOC changes have been demonstrated to be the main controlling factor of North Atlantic SST during the Heinrich-like stadials that punctuate glacial terminations[146]. In particular, the SST records from Iberian Margin core[60] MD01-2443 and from IODP Site U1313 in the North Atlantic IRD belt[147] are ideally suited for inferring variability in the AMOC. The SST variations at these sites reflect oscillations of the Arctic Front and the interactions between colder polar and warmer subtropical waters during glacial–interglacial cycles[147]. These dynamics are strongly modulated by the strength and position of the North Atlantic Current (NAC), a key component of the upper limb of the AMOC and of the associated northward heat transport[60,61,142,147,148]. During the Heinrich-like stadials of glacial terminations, a weakening of both the AMOC and the NAC reduces the northward transport of warm waters, cooling the SST in regions (e.g. the Iberian Margin) sensitive to northward heat transport in the eastern North Atlantic (e.g. refs. 37,149). Consequently, Iberian Margin SST cooling during glacial terminations is associated with a weak AMOC state.

To ensure that all records are placed on an absolute chronology, we selected sites where T-I and T-II are radiometrically constrained. For T-I, we employed the $^{231}Pa/^{230}Th$ ratio as an indicator of AMOC strength of Ocean Drilling Program (ODP) Site 1063 (Supplementary Fig. 9a), for which a radiocarbon-based chronology is available[66]. Lower $^{231}Pa/^{230}Th$ values indicate a strong AMOC, while higher values indicate a weakened or collapsed AMOC[1]. For T-II, where the resolution of $^{231}Pa/^{230}Th$ records is low and lacks a radiometric age control, we used a combination of εNd[150]) from ODP Site 1063 and the SST record from core MD01-2444 (Iberian Margin)[34,151] as AMOC indicators (Supplementary Fig. 10a, b). The chronology of MD01-2444 was radiometrically constrained using Mediterranean speleothems[34], providing an independent basis to complement the ODP 1063 record, which relied on tuning with an ice-core chronology[150] that is consistent with radiometric age constraints[34]. The εNd signature reflects water mass provenance and mixing, as the contrast between the unradiogenic North Atlantic Deep Water and the more radiogenic Southern Source Waters allows reconstructing shifts in deep-water composition and circulation patterns[152].

For T-III, we focused on SST records from Iberian Margin core[153] MD01-2443, recovered at the same location as MD01-2444, and complement these data with $\delta^{13}C$ records from Ejulve Cave[36]. Given the similar response of SST to AMOC variability observed at MD01-2444 during T-II, we consider the SST records at MD01-2443 well-suited for inferring changes in AMOC strength (Supplementary Fig. 11a). For T-V, we utilised SST from marine core[147] Site U1313 in the central Atlantic as the primary AMOC indicator (Supplementary Fig. 13b), where the presence of IRD (Supplementary Fig. 13a) indicates the prevalent ice-sheet melt that was usually accompanied by AMOC slowdown[147,148].

The use of εNd and North Atlantic SST as alternative AMOC proxies was validated by comparison with the well-resolved $^{231}Pa/^{230}Th$ record for T-I (Supplementary Fig. 9a–c), for which independent absolute chronologies can be constructed. This analysis reveals a close correspondence between εNd variations[66,154] at ODP Site 1063/OCE326-GGC6 and the SST anomalies from the precisely radiocarbon-dated core MD95-2042 (ref. 142) with AMOC changes inferred from the Pa/Th proxy. Change-point analysis of the proxy time series using the BREAKFIT algorithm[65] further corroborates this relationship: the onset of SST cooling in MD95-2042 occurred at 17.8 ± 1.0 kyr BP (2σ), while the AMOC slowdown based on $^{231}Pa/^{230}Th$ at ODP Site 1063/OCE326-GGC6 initiated at 18.1 ± 1.0 kyr BP (2σ). This analysis validates the use of εNd and/or SST time series to pinpoint AMOC slowdowns during the Heinrich-like stadials of earlier terminations (T-II through T-V).

Duration between the onset of the AMOC slowdown and the meltwater pulse

Termination I (T-I). As reported above, BREAKFIT analysis[65] of $^{231}Pa/^{230}Th$ ratios from ODP Site 1063 (Supplementary Fig. 1) in the western North Atlantic[66] constrains the onset of AMOC slowdown associated with the Heinrich stadial 1 during T-I to 18.1 ± 1.0 kyr BP (Supplementary Fig. 9a). The chronology of ODP Site 1063 is ^{14}C-based, with associated 2σ uncertainties within several hundred years. In our analysis, we took a conservative stance and expanded the 2σ chronological uncertainties to 1 kyr. The timing of the onset of the AMOC slowdown at ODP Site 1063 coincides with the onset of a weak monsoon interval recorded in the radiometrically dated Chinese speleothems at ~18 kyr BP (Supplementary Fig. 9d)[2].

The highest rates of sea-level rise in the Red Sea records occurred at 11.4 ± 1.0 kyr BP[10]), aligning with Meltwater Pulse 1B (MWP 1B; ref. 11). However, the reliability of sea-level reconstructions from the Red Sea records through the 14–23 kyr BP interval is limited by the low sampling resolution and/or the presence of gaps in the records[10,67,68] caused by the so-called 'aplanktonic zones'. An earlier and more pronounced global sea-level rise during T-I was documented at ~14.7 kyr BP, termed 'Meltwater Pulse 1A' (MWP 1A)[63]. In this study, we use the global mean sea level (GMSL) record by Lambeck et al. (ref. 11) for T-I. We applied a 500-year Gaussian filter to Lambeck's sea-level reconstruction and used 5000 Monte-Carlo simulations to compute the first derivative of the time series and obtain the rates of sea-level change (with the median and 95% confidence level). This method mirrors Grant et al. (ref. 10), who used the same filter to minimise the influence of spurious data in the computation of the rates of change. Accordingly, the method used to compute the rates of sea-level change across T-I is consistent with that used for the other glacial terminations[10] (T-II to T-V) investigated in this study. Our analysis suggests that the rates of change computed from the GMSL time series attained a distinct maximum of 24.6–26.2 m kyr^{-1} (95% confidence level) at 14.1 ± 1.0 kyr BP (Supplementary Fig. 9e, g). This data analysis indicates that the onset of the AMOC slowdown led maximum rates of sea-level rise by 4.0 ± 1.4 kyr (2σ) during T-I.

Termination II (T-II). SST time series from the Iberian Margin MD01-2444 (Supplementary Fig. 1), on their published radiometrically constrained chronology[34], are used to determine the onset of the AMOC slowdown during T-II. Warm planktic foraminiferal percentages and εNd from ODP Site 1063 (ref. 150) support the link between AMOC slowdown and pronounced SST cooling[34,151] in the North Atlantic during T-II (Supplementary Fig. 10a). BREAKFIT analysis[65] of the SST record from MD01-2444 indicates that the onset of AMOC slowdown during T-II occurs at 135.5 ± 1.2 kyr BP. This timing coincides with the onset of Heinrich stadial 11 in a radiometrically constrained chronology that was validated by multiple speleothems[34] (Supplementary Fig. 10b). The timing determined here for the initial AMOC slowdown of T-II coincides within uncertainties with the onset of the weak monsoon interval of T-II at 136.0 ± 1.0 kyr BP in the radiometrically dated Chinese speleothems[2] (Supplementary Fig. 10c). Maximum rates of sea-level rise in the Red Sea records occurred during the second phase of Heinrich stadial 11 (ref. 34), at 132.6 ± 0.7 kyr BP (ref. 10;

 https://doi.org/10.1038/s41467-026-73733-6

Supplementary Fig. 10d, e). This analysis indicates that the onset of the AMOC slowdown led the maximum rates of sea-level rise by 2.9 ± 1.4 kyr (2σ) during T-II.

Termination III (T-III). There is to date no marine record spanning T-III for which a radiometrically constrained chronology has been presented. Here we relied on the coupling of Spanish speleothems (Ejulve cave) δ^{13}C and North Atlantic cooling at 250–240 kyr BP (ref. 36) to transfer radiometric constraints from U-Th-dated speleothems to Iberian Margin core MD01-2443 (Supplementary Fig. 1). The Ejulve cave's chronology[36]) was synchronised to MD01-2443 SST record, which is derived with the SIMMAX planktonic-foraminifera transfer function[153]). For the synchronisation, we used four tie-points at 257.4 ± 3.0, 249.4 ± 2.3, 240.9 ± 2.3, and 229.7 ± 2.4 kyr BP (Supplementary Fig. 11a, b). The oldest and youngest tie points were taken from the original MD01-2443 age model[153], while the others were identified at the onset and end of low SST periods that are assumed to coincide with the marked increase and final major decrease in Ejulve δ^{13}C, respectively[36]. Chronological uncertainties are rigorously and fully propagated, following the approach reported for IODP Site U1385.

BREAKFIT analysis[65] places the onset of the AMOC slowdown (SST drop) of the Heinrich-like stadial of T-III at 250.1 ± 4.0 kyr BP, which aligns with the onset of a weak monsoon interval at 250.4 ± 0.5 kyr BP in the radiometrically dated Chinese speleothems (ref. 2, Supplementary Fig. 11c). Maximum rates of sea-level rise in the Red Sea records occur at 241.3 ± 0.5 kyr BP (Supplementary Fig. 11d, e). It is worth noting that the Ejulve cave δ^{13}C time series shows two millennial-scale cooling events[36] during T-III, which commenced at ~250 and ~245 kyr BP. Our analysis centres on the timing of the oldest stadial, because SST time series from the Iberian Margin (Supplementary Fig. 11a) do not document the occurrence of a clear interstadial (hence an AMOC resumption) between 250 and 239 kyr BP. Based on this analysis and its underlying assumptions, the interval between the onset of the AMOC slowdown and the timing of the meltwater pulse of T-III lasted 8.8 ± 4.0 kyr BP.

Termination IV (T-IV). BREAKFIT analysis[65] applied to the SST record from Site U1385, based on the new radiometrically constrained chronology presented here, places the onset of the AMOC slowdown of T-IV at 346.5 ± 2.5 kyr BP. Considering the maximum rates of sea-level rise in the Red Sea records at 333.6 ± 0.6 kyr BP, this analysis constrains the duration of the interval between the onset of the AMOC slowdown and the timing of the maximum rates of sea-level rise during T-IV to 12.9 ± 2.7 kyr.

Termination V (T-V). For T-V, we target the SST time series from North Atlantic IODP Site U1313 (41°00′N, 32°57′W, 3,426 m water depth; Supplementary Fig. 1) on its recently published radiometrically constrained chronology[31]. This was obtained through synchronisation with Bàsura cave, with the associated chronological uncertainties that were rigorously propagated. The Bàsura-based chronology places at 433.5 ± 4.0 kyr BP the onset of the AMOC slowdown of T-V (Supplementary Fig. 13a, b), which coincides within uncertainties with the onset of a weak monsoon interval at 430.9 ± 1.5 kyr BP in the radiometrically dated Chinese speleothems (Supplementary Fig. 13c)[47]. Given that the maximum rates of sea level rise of T-V in the Red Sea records occur at 428.8 ± 3.8 kyr BP (Supplementary Fig. 13d, f), the interval between the onset of the AMOC slowdown and the timing of the meltwater pulse of T-V lasted 4.7 ± 5.5 kyr.

Change rates in the benthic δ^{18}O ($\delta^{18}O_b$) stack

The rates of $\delta^{18}O_b$ change in the North Atlantic stack[7] were calculated by Monte Carlo analysis using their chronological and proxy-related uncertainties, employing Gaussian filters of 0.5 kyr. North Atlantic $\delta^{18}O_b$ was considered as an indicator of global ice volume, with high $\delta^{18}O_b$ corresponding to large ice volumes. $\delta^{18}O_b$ change rates can therefore be used to evaluate the rapidity of ice collapse and/or sea-level rise, in line with the work of ref. 7. Given the inverse relationship, we identify the timing of maximum sea-level rise rates where minimum $\delta^{18}O_b$ change rates were observed.

Climate models

Subsurface ocean warming and heat uptake during periods of changing AMOC strength are investigated from the outputs of: (a) the iTraCE transient simulations[71]; (b) the NCAR Community Climate System Model version 3 (CCSM3)[22]; and (c) the Coupled Model Intercomparison Project Phase 6 (CMIP6).

iTraCE. iTraCE is driven by ice-sheet (ice), orbital (orb), greenhouse-gas (ghg), and meltwater (wtr) forcings. Three sensitivity experiments were compared: ice–ghg–orb–wtr (all forcings), ice–ghg–orb (excluding meltwater), and ice–orb (excluding both GHG and meltwater). We evaluated North Atlantic ocean heat content (OHC; derived following ref. 155) in the iTraCE transient simulation[71,156] during T-I (Supplementary Fig. 7). The interval 11–20 kyr BP was analysed by integrating temperature over the upper 0–2000 m within 0–45°N, 90°W–0°. Only the experiment that includes meltwater forcing simulated a pronounced AMOC slowdown and an OHC increase of approximately 40–45 GJ m^{-2} (Supplementary Fig. 7a, b) during the Heinrich Stadial 1 (~18–15 kyr BP) and Younger Dryas (~13–12 kyr BP). The absence of a comparable OHC rise in the ice–ghg–orb and ice–orb experiments (Supplementary Fig. 7c) further underscores that heat accumulation is a robust response to freshwater-driven AMOC weakening, thereby corroborating the analysis based on proxy data and the proposed heat-storage-and-release mechanism during glacial terminations.

CMIP6. CMIP6 provides a coordinated framework of fully coupled Earth System Models that incorporate atmosphere, ocean, land, sea ice, and biogeochemical components, and is widely used for assessing future climate projections under different Shared Socioeconomic Pathways (SSPs)[78]. The three SSPs analysed here span a broad range of radiative forcing trajectories by 2100: (i) SSP1-2.6 represents a strong mitigation scenario with peak-and-decline CO_2 emissions; (ii) SSP2-4.5 represents an intermediate stabilisation pathway; and (iii) SSP5-8.5 represents a fossil-fuel intensive 'high-emissions' scenario. These scenarios correspond to effective radiative forcings of ~2.6, 4.5, and 8.5 W m^{-2}, with atmospheric CO_2 concentrations ranging from ~420–490 ppm (SSP1-2.6) to >1000 ppm (SSP5-8.5).

We examined the relationship between changes in the AMOC strength (in Sv) and the basin-integrated OHC in 19 CMIP6 models for 2015–2100 CE under the SSP1-2.6, SSP2-4.5, and SSP5-8.5 scenarios. Across all models and scenarios, changes in AMOC strength correlate strongly and inversely with OHC ($r = -0.73$, $p < 0.05$; Supplementary Fig. 8), indicating that a weakened AMOC is systematically accompanied by enhanced subsurface warming and basin-scale OHC. The robustness of this inverse correlation across a large ensemble of models and forcing pathways suggests that ocean heat uptake and storage are tightly coupled to AMOC dynamics, reinforcing the potential for ocean circulation changes to modulate future sea-level rise and cryospheric response.

CCSM3. The NCAR CCSM3 is a fully coupled atmosphere–ocean–sea ice–land general circulation model, widely used in paleoclimate research for transient simulations of glacial–interglacial cycles. The transient experiments analysed here follow the design of the TraCE-21k simulation[77] for T-I, and its extension to T-II and last interglacial[22]. Supplementary Fig. 12 presents the temperature response of uppermost 1000 m in the North Atlantic Ocean during T-I and T-II. Subsurface warming (Supplementary Fig. 12b) intensifies as the AMOC

https://doi.org/10.1038/s41467-026-73733-6

weakens (Supplementary Fig. 12a). The periods where the rates of sea-level rise peak (~14.2 kyr BP for T-I and ~132.6 kyr BP for T-II; Supplementary Fig. 12c) align with the modelled AMOC recovery and a brief episode of surface warming, plausibly induced by upward heat transfer.

Deep-ocean temperature and oceanic heat content

The energy accumulated within the ocean during terminations was estimated using the deep-ocean temperature (DOT) reconstructions from Rohling et al.[83] (Fig. 4c; Supplementary Figs. 9e, 10e, 11e and 13d). DOT change is considered a reliable proxy for mean ocean temperature (MOT) change, because over the multimillennial timescales of ocean mixing, DOT changes reflect large-scale modifications in ocean heat content[83]. DOT changes during terminations were compared with noble-gas-derived MOT records from ice cores where the two reconstructions overlap (Fig. 4c; Supplementary Figs. 9e, 10e, 11e). Uncertainty in the DOT estimates was set to ±0.5 °C (2σ), which is comparable to the uncertainties observed in the noble-gas-derived MOT[69] and the natural variability among different ice cores[79].

The ocean heat content anomaly (ΔOHC) was calculated following Baggenstos et al. [79]:

$$\Delta\mathrm{OHC} = \Delta T \times C_\mathrm{p} \times M \quad (1)$$

where ΔT is the change in DOT (°C), C_p is the specific heat capacity of seawater (4,184 J/[kg °C]), and M is the mass of the ocean (1.335×10^{21} kg; ref. 79). Given that the heat capacity of seawater and the mass of the ocean are assumed to remain constant through time, the uncertainty in the energy estimate is dominated by the errors in the DOT estimate (±0.5 °C, 2σ), which corresponds to approximately $\pm 2.8 \times 10^{24}$ J (2σ). Monte Carlo simulations (5000 ensembles total; 1000 per termination from T-I to T-V) were performed to evaluate the correlation between ocean heat content and duration of the episodes of AMOC slowdown during the last five glacial terminations (Fig. 5c).

Ice sheet evolution and source(s) of meltwater during Termination IV (T-IV)

To evaluate the ice-sheet evolution and the potential sources of meltwater during T-IV, we examined two independent reconstructions of the volume of individual ice sheets derived from composite, global benthic δ^{18}O stack[6], based on recent numerical solutions[83] and another from model simulations[93] (Supplementary Fig. 14). To ensure comparability within a consistent chronological framework and coherent sea-level change patterns, we aligned both ice-sheet volume reconstructions with the radiometrically constrained Red Sea relative sea-level (RSL) record[10] following the methodology in Rohling et al.[83] (Supplementary Fig. 14a).

The reconstructions suggest that during the earliest part of T-IV (~346 to ~342 kyr BP), both Laurentide Ice Sheet (LIS) and Eurasian Ice Sheet (EIS) have expanded slightly, resulting in lowered global sea levels (Supplementary Fig. 14b, c). Over the subsequent ~8 kyr, despite some discrepancies in the precise timing of the major deglacial ice-sheet retreat, the individual ice-sheet reconstructions considered here[83,93] indicate an overall ice mass loss from the LIS and EIS of ~40–50% relative to their volumes at the preceding glacial maximum (Supplementary Fig. 14b, c). Specifically, the LIS and EIS lost sea-level equivalents (s.l.e.) of ~20 m and ~10 m, respectively. Meanwhile, the Antarctic Ice Sheet (AIS) experienced a more modest reduction of about 10% (~5 m s.l.e.), whereas changes in the Greenland Ice Sheet were negligible. Collectively, these ice-sheet losses correspond to meltwater volumes of roughly 1.1×10^{16} m^3 and 1.8×10^{15} m^3 from the Northern Hemisphere and Southern Hemisphere ice sheets.

The rates of sea-level rise peaked at ~334 kyr BP[10], with the melting of the LIS and EIS contributing approximately 40–50 m s.l.e., and the AIS adding another ~5–10 m s.l.e. This corresponds to meltwater discharge volumes of ~1.5–1.8×10^{16} m^3 from the Northern Hemisphere ice sheets and ~1.8–3.6×10^{15} m^3 from the AIS. These reconstructions thus suggest that the rapid sea-level rise at the end of T-IV was predominantly driven by the collapse of Northern Hemisphere ice sheets, with a secondary contribution from Antarctic melting.

Data availability

Supplementary Data 1 to 6 are provided in the Supplementary Information.

References

1. McManus, J. F., Francois, R., Gherardi, J. M., Keigwin, L. D. & Brown-Leger, S. Collapse and rapid resumption of Atlantic meridional circulation linked to deglacial climate changes. *Nature* **428**, 834–837 (2004).
2. Cheng, H. et al. Ice age terminations. *Science* **326**, 248–252 (2009).
3. Clark, P. U. et al. Global climate evolution during the last deglaciation. *Proc. Natl. Acad. Sci. USA* **109**, E1134–E1142 (2012).
4. Broecker, W. S. & von Donk, J. Insolation changes, ice volumes, and the δ^{18}O record in deep-sea cores. *Rev. Geophys*. **8**, 169–198 (1970).
5. Broecker, W. S. Terminations. in *Milankovitch and Climate* (eds Berger, A., Imbrie, J., Hays, J., Kukla, G. & Saltzman, B.) 687–698 (Springer, 1984).
6. Lisiecki, L. E. & Raymo, M. E. A Pliocene-Pleistocene stack of 57 globally distributed benthic δ^{18}O records. *Paleoceanography* **20**, PA1003 (2005).
7. Hobart, B., Lisiecki, L. E., Rand, D., Lee, T. & Lawrence, C. E. Late Pleistocene 100-kyr glacial cycles paced by precession forcing of summer insolation. *Nat. Geosci.* **16**, 717–722 (2023).
8. Cutler, K. B. et al. Rapid sea-level fall and deep-ocean temperature change since the last interglacial period. *Earth Planet. Sci. Lett.* **206**, 253–271 (2003).
9. Thomas, A. L. et al. Penultimate deglacial sea-level timing from uranium/thorium dating of Tahitian corals. *Science* **324**, 1186–1189 (2009).
10. Grant, K. M. et al. Sea-level variability over five glacial cycles. *Nat. Commun.* **5**, 5076 (2014).
11. Lambeck, K., Rouby, H., Purcell, A., Sun, Y. & Sambridge, M. Sea level and global ice volumes from the Last Glacial Maximum to the Holocene. *Proc. Natl. Acad. Sci. USA* **111**, 15296–15303 (2014).
12. Elderfield, H. et al. Evolution of ocean temperature and ice volume through the mid-Pleistocene climate transition. *Science* **337**, 704–709 (2012).
13. Spratt, R. M. & Lisiecki, L. E. A Late Pleistocene sea level stack. *Clim. Past* **12**, 1079–1092 (2016).
14. Fairbanks, R. B., Charles, C. D. & Wright, J. D. Origin of global meltwater pulses. in *Radiocarbon After Four Decades* (eds Taylor, R. E., Long, A. & Kra, R. S.) 473–500 (Springer, 1992).
15. McManus, J. F., Oppo, D. W. & Cullen, J. L. A 0.5-million-year record of millennial-scale climate variability in the North Atlantic. *Science* **283**, 971–975 (1999).
16. Hodell, D. A. et al. A 1.5-million-year record of orbital and millennial climate variability in the North Atlantic. *Clim. Past* **19**, 607–636 (2023).
17. Zhang, X., Knorr, G., Lohmann, G. & Barker, S. Abrupt North Atlantic circulation changes in response to gradual CO_2 forcing in a glacial climate state. *Nat. Geosci.* **10**, 518–523 (2017).
18. Barker, S. & Knorr, G. Millennial scale feedbacks determine the shape and rapidity of glacial termination. *Nat. Commun.* **12**, 2273 (2021).
19. Denton, G. H. et al. The last glacial termination. *Science* **328**, 1652–1656 (2010).

20. Carlson, A. E. & Clark, P. U. Ice sheet sources of sea level rise and freshwater discharge during the last deglaciation. *Rev. Geophys.* **50**, RG4007 (2012).
21. Alley, R. B., Clark, P. U., Huybrechts, P. & Joughin, I. Ice-sheet and sea-level changes. *Science* **310**, 456–460 (2005).
22. Gregoire, L. J., Payne, A. J. & Valdes, P. J. Deglacial rapid sea level rises caused by ice-sheet saddle collapses. *Nature* **487**, 219–222 (2012).
23. Gregoire, L. J., Otto-Bliesner, B., Valdes, P. J. & Ivanovic, R. Abrupt Bølling warming and ice saddle collapse contributions to the Meltwater Pulse 1a rapid sea level rise. *Geophys. Res. Lett.* **43**, 9130–9137 (2016).
24. Reyes, A. V. et al. Timing of Cordilleran-Laurentide ice-sheet separation: Implications for sea-level rise. *Quat. Sci. Rev.* **328**, 108554 (2024).
25. Clark, P. U. et al. Oceanic forcing of penultimate deglacial and last interglacial sea-level rise. *Nature* **577**, 660–664 (2020).
26. Scholz, D. & Hoffmann, D. L. StalAge – An algorithm designed for construction of speleothem age models. *Quat. Geochronol.* **6**, 369–382 (2011).
27. Hu, H. M. et al. Tracking westerly wind directions over Europe since the middle Holocene. *Nat. Commun.* **13**, 7866 (2022).
28. Rohling, E. J., Marino, G. & Grant, K. M. Mediterranean climate and oceanography, and the periodic development of anoxic events (sapropels). *Earth Sci. Rev.* **143**, 62–97 (2015).
29. Pinto, J. G. et al. Identification and ranking of extraordinary rainfall events over Northwest Italy: The role of Atlantic moisture. *J. Geophys. Res. Atmos.* **118**, 2085–2097 (2013).
30. Lionello, P., Giorgi, F., Rohling, E. J. & Seager, R. Mediterranean climate: past, present and future. in *Oceanography of the Mediterranean Sea: An Introductory Guide* (eds Schroeder, K. & Chiggiato, J.) 41–91 (Elsevier, 2023).
31. Hu, H. M. et al. Sustained North Atlantic warming drove anomalously intense MIS 11c interglacial. *Nat. Commun.* **15**, 5933 (2024).
32. Desprat, S. et al. Millennial-scale climate variability potentially shaped the early interglacial optimum in southern Europe. *Paleoceanogr. Paleoclimatol.* **39**, e2024PA004846 (2024).
33. Rodrigues, T. et al. A 1-Ma record of sea surface temperature and extreme cooling events in the North Atlantic: a perspective from the Iberian Margin. *Quat. Sci. Rev.* **172**, 118–130 (2017).
34. Marino, G. et al. Bipolar seesaw control on last interglacial sea level. *Nature* **522**, 197–201 (2015).
35. Stoll, H. M. et al. Rapid northern hemisphere ice sheet melting during the penultimate deglaciation. *Nat. Commun.* **13**, 3819 (2022).
36. Pérez-Mejías, C. et al. Abrupt climate changes during Termination III in Southern Europe. *Proc. Natl. Acad. Sci. USA* **114**, 10047–10052 (2017).
37. Ivanovic, R. F. et al. Acceleration of northern ice sheet melt induces AMOC slowdown and northern cooling in simulations of the early last deglaciation. *Paleoceanogr. Paleoclimatol.* **33**, 807–824 (2018).
38. Kageyama, M. et al. Climatic impacts of fresh water hosing under Last Glacial Maximum conditions: a multi-model study. *Clim. Past* **9**, 935–953 (2013).
39. Ziemen, F. A., Kapsch, M. L., Klockmann, M. & Mikolajewicz, U. Heinrich events show two-stage climate response in transient glacial simulations. *Clim. Past* **15**, 153–168 (2019).
40. Fairchild, I. J. & Treble, P. C. Trace elements in speleothems as recorders of environmental change. *Quat. Sci. Rev.* **28**, 449–468 (2009).
41. Hu, H. M. et al. Split westerlies over Europe in the early Little Ice Age. *Nat. Commun.* **13**, 4898 (2022).
42. Sassoon, D. et al. Pollen-based climatic reconstructions for the interglacial analogues of MIS 1 (MIS 19, 11, and 5) in the south-western Mediterranean: insights from ODP Site 976. *Clim. Past* **21**, 489–515 (2025).
43. Nehrbass-Ahles, C. et al. Abrupt CO_2 release to the atmosphere under glacial and early interglacial climate conditions. *Science* **369**, 1000–1005 (2020).
44. Zhang, H. et al. Iberian Margin surface ocean cooling led freshening during Marine Isotope Stage 6 abrupt cooling events. *Nat. Commun.* **14**, 5390 (2023).
45. Meckler, A. N., Clarkson, M. O., Cobb, K. M., Sodemann, H. & Adkins, J. F. Interglacial hydroclimate in the tropical west Pacific through the late Pleistocene. *Science* **336**, 1301–1304 (2012).
46. Bischoff, T., Schneider, T. & Meckler, A. N. A conceptual model for the response of tropical rainfall to orbital variations. *J. Clim.* **30**, 8375–8391 (2017).
47. Cheng, H. et al. The Asian monsoon over the past 640,000 years and ice age terminations. *Nature* **534**, 640–646 (2016).
48. Wang, X. et al. Wet periods in northeastern Brazil over the past 210 kyr linked to distant climate anomalies. *Nature* **432**, 740–743 (2004).
49. Gibbons, F. T. et al. Deglacial $\delta^{18}O$ and hydrologic variability in the tropical Pacific and Indian Oceans. *Earth Planet. Sci. Lett.* **387**, 240–251 (2014).
50. Torner, J. et al. New age constraints for glacial terminations IV, III, and III.a based on western Mediterranean speleothem records. *Clim. Past* **21**, 465–487 (2025).
51. Marra, F., Florindo, F., Anzidei, M. & Sepe, V. Paleo-surfaces of glacio-eustatically forced aggradational successions in the coastal area of Rome: assessing interplay between tectonics and sea-level during the last ten interglacials. *Quat. Sci. Rev.* **148**, 85–100 (2016).
52. Laskar, J., Fienga, A., Gastineau, M. & Manche, H. La2010: a new orbital solution for the long-term motion of the Earth. *Astron. Astrophys.* **532**, A89 (2011).
53. Raymo, M. E. The timing of major climate terminations. *Paleoceanography* **12**, 577–585 (1997).
54. Milanković, M. *Kanon der Erdbestrahlung und seine Anwendung auf das Eiszeitenproblem* (Royal Serbian Academy, 1941).
55. Jouzel, J. et al. Orbital and millennial Antarctic climate variability over the past 800,000 years. *Science* **317**, 793–796 (2007).
56. Barbante, C. et al. One-to-one coupling of glacial climate variability in Greenland and Antarctica. *Nature* **444**, 195–198 (2006).
57. Shin, J. et al. Millennial-scale atmospheric CO_2 variations during the Marine Isotope Stage 6 period (190–135 ka). *Clim. Past* **16**, 2203–2219 (2020).
58. Pedro, J. B. et al. Beyond the bipolar seesaw: toward a process understanding of interhemispheric coupling. *Quat. Sci. Rev.* **192**, 27–46 (2018).
59. Zhu, C. et al. Antarctic warming during Heinrich Stadial 1 in a transient isotope-enabled deglacial simulation. *J. Clim.* **35**, 7353–7365 (2022).
60. Rodrigues, T., Voelker, A. H. L., Grimalt, J. O., Abrantes, F. & Naughton, F. Iberian Margin sea surface temperature during MIS 15 to 9 (580–300 ka): Glacial suborbital variability versus interglacial stability. *Paleoceanography* **26**, PA1204 (2011).
61. Martin-Garcia, G. M., Sierro, F. J., Flores, J. A. & Abrantes, F. Change in the North Atlantic circulation associated with the mid-Pleistocene transition. *Clim. Past* **14**, 1639–1651 (2018).
62. Stanford, J. D. et al. A new concept for the paleoceanographic evolution of Heinrich event 1 in the North Atlantic. *Quat. Sci. Rev.* **30**, 1047–1066 (2011).
63. Deschamps, P. et al. Ice-sheet collapse and sea-level rise at the Bølling warming 14,600 years ago. *Nature* **483**, 559–564 (2012).

64. Hodell, D. A. et al. Anatomy of Heinrich Layer 1 and its role in the last deglaciation. *Paleoceanography* **32**, 284–303 (2017).
65. Mudelsee, M. Break function regression. *Eur. Phys. J. Spec. Top.* **174**, 49–63 (2009).
66. Böhm, E. et al. Strong and deep Atlantic Meridional Overturning Circulation during the last glacial cycle. *Nature* **517**, 73–76 (2015).
67. Fenton, M., Geiselhart, S., Rohling, E. J. & Hemleben, C. Aplanktonic zones in the Red Sea. *Mar. Micropaleontol.* **40**, 277–294 (2000).
68. Grant, K. M. et al. Rapid coupling between ice volume and polar temperature over the past 150,000 years. *Nature* **491**, 744–747 (2012).
69. Bereiter, B., Shackleton, S., Baggenstos, D., Kawamura, K. & Severinghaus, J. Mean global ocean temperatures during the last glacial transition. *Nature* **553**, 39–44 (2018).
70. Grimmer, M. et al. AMOC modulates ocean heat content during deglaciations. *Geophys. Res. Lett.* **52**, e2024GL114415 (2025).
71. He, C. et al. Hydroclimate footprint of pan-Asian monsoon water isotope during the last deglaciation. *Sci. Adv.* **7**, eabe2611 (2021).
72. Marcott, S. A. et al. Ice-shelf collapse from subsurface warming as a trigger for Heinrich events. *Proc. Natl. Acad. Sci. USA* **108**, 13415–13419 (2011).
73. Alvarez-Solas, J., Robinson, A., Montoya, M. & Ritz, C. Iceberg discharges of the last glacial period driven by oceanic circulation changes. *Proc. Natl. Acad. Sci. USA* **110**, 16350–16354 (2013).
74. He, C. et al. North Atlantic subsurface temperature response controlled by effective freshwater input in "Heinrich" events. *Earth Planet. Sci. Lett.* **539**, 116247 (2020).
75. Max, L., Nürnberg, D., Chiessi, C. M., Lenz, M. M. & Mulitza, S. Subsurface ocean warming preceded Heinrich Events. *Nat. Commun.* **13**, 4217 (2022).
76. Rasmussen, T. L. & Thomsen, E. Warm Atlantic surface water inflow to the Nordic seas 34-10 calibrated ka B.P. *Paleoceanography* **23**, PA1201 (2008).
77. Liu, Z. et al. Transient simulation of last deglaciation with a new mechanism for Bolling-Allerød warming. *Science* **325**, 310–314 (2009).
78. Eyring, V. et al. Overview of the Coupled Model Intercomparison Project Phase 6 (CMIP6) experimental design and organization. *Geosci. Model Dev.* **9**, 1937–1958 (2016).
79. Baggenstos, D. et al. Earth's radiative imbalance from the Last Glacial Maximum to the present. *Proc. Natl. Acad. Sci. USA* **116**, 14881–14886 (2019).
80. Shackleton, S. et al. Global ocean heat content in the Last Interglacial. *Nat. Geosci.* **13**, 77–81 (2020).
81. Shackleton, S., Seltzer, A., Baggenstos, D. & Lisiecki, L. E. Benthic $\delta^{18}O$ records Earth's energy imbalance. *Nat. Geosci.* **16**, 797–802 (2023).
82. Rohling, E. J. et al. Sea level and deep-sea temperature reconstructions suggest quasi-stable states and critical transitions over the past 40 million years. *Sci. Adv.* **7**, eabf5326 (2021).
83. Rohling, E. J. et al. Comparison and synthesis of sea-level and deep-sea temperature variations over the past 40 million years. *Rev. Geophys.* **60**, e2022RG000775 (2022).
84. Hill, E. A., Gudmundsson, G. H. & Chandler, D. M. Ocean warming as a trigger for irreversible retreat of the Antarctic ice sheet. *Nat. Clim. Change* **14**, 1165–1171 (2024).
85. Galbraith, E. D., Merlis, T. M. & Palter, J. B. Destabilization of glacial climate by the radiative impact of Atlantic Meridional Overturning Circulation disruptions. *Geophys. Res. Lett.* **43**, 8214–8221 (2016).
86. Thiagarajan, N., Subhas, A. V., Southon, J. R., Eiler, J. M. & Adkins, J. F. Abrupt pre-Bølling-Allerød warming and circulation changes in the deep ocean. *Nature* **511**, 75–78 (2014).
87. Wu, P., Jackson, L., Pardaens, A. & Schaller, N. Extended warming of the northern high latitudes due to an overshoot of the Atlantic Meridional Overturning Circulation. *Geophys. Res. Lett.* **38**, L24704 (2011).
88. Myhre, G., Highwood, E. J., Shine, K. P. & Stordal, F. New estimates of radiative forcing due to well mixed greenhouse gases. *Geophys. Res. Lett.* **25**, 2715–2718 (1998).
89. Noël, B., van de Berg, W. J., Lhermitte, S. & van den Broeke, M. R. Rapid ablation zone expansion amplifies north Greenland mass loss. *Sci. Adv.* **5**, eaaw0123 (2019).
90. Scambos, T. A., Hulbe, C., Fahnestock, M. & Bohlander, J. The link between climate warming and break-up of ice shelves in the Antarctic Peninsula. *J. Glaciol.* **46**, 516–530 (2000).
91. Scambos, T. A., Bohlander, J. A., Shuman, C. A. & Skvarca, P. Glacier acceleration and thinning after ice shelf collapse in the Larsen B embayment, Antarctica. *Geophys. Res. Lett.* **31**, L18402 (2004).
92. Massom, R. A. et al. Antarctic ice shelf disintegration triggered by sea ice loss and ocean swell. *Nature* **558**, 383–389 (2018).
93. de Boer, B., Lourens, L. J. & van de Wal, R. S. W. Persistent 400,000-year variability of Antarctic ice volume and the carbon cycle is revealed throughout the Plio-Pleistocene. *Nat. Commun.* **5**, 2999 (2014).
94. Rahmstorf, S. Is the Atlantic overturning circulation approaching a tipping point? *Oceanography* **37**, 16–29 (2024).
95. Shen, C. C. et al. Variation of initial $^{230}Th/^{232}Th$ and limits of high precision U–Th dating of shallow-water corals. *Geochim. Cosmochim. Acta* **72**, 4201–4223 (2008).
96. Shen, C. C. et al. High-precision and high-resolution carbonate ^{230}Th dating by MC-ICP-MS with SEM protocols. *Geochim. Cosmochim. Acta* **99**, 71–86 (2012).
97. Cheng, H. et al. Improvements in ^{230}Th dating, ^{230}Th and ^{234}U half-life values, and U-Th isotopic measurements by multi-collector inductively coupled plasma mass spectrometry. *Earth Planet. Sci. Lett.* **371–372**, 82–91 (2013).
98. Hu, H. M. et al. Sub-epsilon natural $^{234}U/^{238}U$ measurements refine the ^{234}U half-life and U-Th geochronology. *Sci. Adv.* **11**, eadu8117 (2025).
99. Jaffey, A. H. et al. Precision measurement of half-lives and specific activities of ^{235}U and ^{238}U. *Phys. Rev. C* **4**, 1889–1906 (1971).
100. Dutton, A. et al. Data reporting standards for publication of U-series data for geochronology and timescale assessment in the earth sciences. *Quat. Geochronol.* **39**, 142–149 (2017).
101. Shen, C. C. et al. High precision measurements of Mg/Ca and Sr/Ca ratios in carbonates by cold plasma inductively coupled plasma quadrupole mass spectrometry. *Chem. Geol.* **236**, 339–349 (2007).
102. Georget, M. et al. Protocol for pollen and dinocyst analysis in marine sediments. protocols.io, https://doi.org/10.17504/protocols.io.x54v92qz4l3e/v1 (2025).
103. Heusser, L. E. Pollen distribution in the bottom sediments of the western North Atlantic Ocean. *Mar. Micropaleontol.* **8**, 77–88 (1983).
104. Janssen, C. R. & Woldringh, R. E. A preliminary radiocarbon dated pollen sequence from the Serra da Estrela, Portugal. *Finisterra* **16**, 299–309 (1981).
105. Maher, L. J. Statistics for microfossil concentration measurements employing samples spiked with marker grains. *Rev. Palaeobot. Palynol.* **32**, 153–191 (1981).
106. Sánchez Goñi, M. F. et al. Moist and warm conditions in Eurasia during the last glacial of the Middle Pleistocene Transition. *Nat. Commun.* **14**, 2700 (2023).
107. Bennett, K. D. Psimpoll and pscomb: computer programs for data plotting and analysis. http://www.kv.geo.uu.se (2000).

108. Birks, H. J. B. & Birks, H. H. *Quaternary Paleoecology* (Edward Arnold, 1980).
109. Juggins, S. rioja: analysis of quaternary science data. R package version 0.87. http://cran.r-project.org/package=rioja (2012).
110. Müller, P. J., Kirst, G., Ruhland, G., von Storch, I. & Rosell-Melé, A. Calibration of the alkenone paleotemperature index $U_{37}^{k'}$ based on core-tops from the eastern South Atlantic and the global ocean (60°N–60°S). *Geochim. Cosmochim. Acta* **62**, 1757–1772 (1998).
111. Villanueva, J., Pelejero, C. & Grimalt, J. O. Clean-up procedures for the unbiased estimation of C_{37} alkenone sea surface temperatures and terrigenous n-alkane inputs in paleoceanography. *J. Chromatogr. A* **757**, 145–151 (1997).
112. Hodell, D. A. et al. The "Shackleton Site" (IODP Site U1385) on the Iberian Margin. *Sci. Drill.* **16**, 13–19 (2013).
113. Shackleton, N. J. The 100,000-year ice-age cycle identified and found to lag temperature, carbon dioxide, and orbital eccentricity. *Science* **289**, 1897–1902 (2000).
114. Stow, D. A. V., Hernández-Molina, F. J., Alvarez-Zarikian, C. A. & Expedition 339 Scientists. In *Proc. IODP* 339 (Integrated Ocean Drilling Program Management International, Inc., 2013).
115. Hodell, D. et al. A reference time scale for Site U1385 (Shackleton Site) on the SW Iberian Margin. *Glob. Planet. Change* **133**, 49–64 (2015).
116. Dorale, J. A. & Liu, Z. Limitations of Hendy test criteria in judging the paleoclimatic suitability of speleothems and the need for replication. *J. Cave Karst Stud.* **71**, 73–80 (2009).
117. Baker, A. et al. Global analysis reveals climatic controls on the oxygen isotope composition of cave drip water. *Nat. Commun.* **10**, 2984 (2019).
118. Dansgaard, W. Stable isotopes in precipitation. *Tellus* **16**, 436–468 (1964).
119. Celle-Jeanton, H., Travi, Y. & Blavoux, B. Isotopic typology of the precipitation in the Western Mediterranean Region at three different time scales. *Geophys. Res. Lett.* **28**, 1215–1218 (2001).
120. Wang, P., Tian, J. & Lourens, L. J. Obscuring of long eccentricity cyclicity in Pleistocene oceanic carbon isotope records. *Earth Planet. Sci. Lett.* **290**, 319–330 (2010).
121. Batchelor, C. L. et al. The configuration of Northern Hemisphere ice sheets through the Quaternary. *Nat. Commun.* **10**, 3713 (2019).
122. Fohlmeister, J. et al. Main controls on the stable carbon isotope composition of speleothems. *Geochim. Cosmochim. Acta* **279**, 67–87 (2020).
123. Hu, H. M. et al. Stalagmite-inferred climate in the western Mediterranean during the Roman Warm Period. *Climate* **10**, 93 (2022).
124. McDermott, F. Palaeo-climate reconstruction from stable isotope variations in speleothems: a review. *Quat. Sci. Rev.* **23**, 901–918 (2004).
125. Genty, D. et al. Timing and dynamics of the last deglaciation from European and North African $\delta^{13}C$ stalagmite profiles—comparison with Chinese and South Hemisphere stalagmites. *Quat. Sci. Rev.* **25**, 2118–2142 (2006).
126. Columbu, A. et al. Speleothem record attests to stable environmental conditions during Neanderthal–modern human turnover in southern Italy. *Nat. Ecol. Evol.* **4**, 1188–1195 (2020).
127. Breecker, D. O. et al. The sources and sinks of CO_2 in caves under mixed woodland and grassland vegetation. *Geochim. Cosmochim. Acta* **96**, 230–246 (2012).
128. Breecker, D. O. Atmospheric pCO_2 control on speleothem stable carbon isotope compositions. *Earth Planet. Sci. Lett.* **458**, 58–68 (2017).
129. Drysdale, R. N. et al. Partitioning of Mg, Sr, Ba and U into a subaqueous calcite speleothem. *Geochim. Cosmochim. Acta* **264**, 67–91 (2019).
130. Fairchild, I. J. et al. Controls on trace element (Sr-Mg) compositions of carbonate cave waters: Implications for speleothem climatic records. *Chem. Geol.* **166**, 255–269 (2000).
131. Ahn, S., Khider, D., Lisiecki, L. E. & Lawrence, C. E. A probabilistic Pliocene–Pleistocene stack of benthic $\delta^{18}O$ using a profile hidden Markov model. *Dyn. Stat. Clim. Syst.* **2**, dzx002 (2017).
132. Konijnendijk, T. Y. M., Ziegler, M. & Lourens, L. J. On the timing and forcing mechanisms of late Pleistocene glacial terminations: Insights from a new high-resolution benthic stable oxygen isotope record of the eastern Mediterranean. *Quat. Sci. Rev.* **129**, 308–320 (2015).
133. Morales-Molino, C. et al. Modern pollen representation of the vegetation of the Tagus Basin (central Iberian Peninsula). *Rev. Palaeobot. Palynol.* **276**, 104193 (2020).
134. Sánchez Goñi, M. F. et al. Climate changes in south western Iberia and Mediterranean Outflow variations during two contrasting cycles of the last 1 Myrs: MIS 31–MIS 30 and MIS 12–MIS 11. *Glob. Planet. Change* **136**, 18–29 (2016).
135. Polunin, O. & Walters, M. *Guide to the Vegetation of Britain and Europe* (Oxford University Press, 1985).
136. Sánchez Goñi, M. F., Eynaud, F., Turon, J. L. & Shackleton, N. J. S. High resolution palynological record off the Iberian margin: direct land-sea correlation for the Last Interglacial complex. *Earth Planet. Sci. Lett.* **171**, 123–137 (1999).
137. Salonen, J. S., Korpela, M., Williams, J. W. & Luoto, M. Machine-learning based reconstructions of primary and secondary climate variables from North American and European fossil pollen data. *Sci. Rep.* **9**, 15805 (2019).
138. Jolliffe, I. T. & Cadima, J. Principal component analysis: a review and recent developments. *Phil. Trans. R. Soc. A* **374**, 20150202 (2016).
139. Sánchez Goñi, M. F. et al. Contrasting impacts of Dansgaard–Oeschger events over a western European latitudinal transect modulated by orbital parameters. *Quat. Sci. Rev.* **27**, 1136–1151 (2008).
140. Budsky, A. et al. Western Mediterranean climate response to Dansgaard/Oeschger events: new insights from speleothem records. *Geophys. Res. Lett.* **46**, 9042–9053 (2019).
141. Barker, S. et al. Interhemispheric Atlantic seesaw response during the last deglaciation. *Nature* **457**, 1097–1102 (2009).
142. Davtian, N. & Bard, E. A new view on abrupt climate changes and the bipolar seesaw based on paleotemperatures from Iberian Margin sediments. *Proc. Natl. Acad. Sci. USA* **120**, e2209558120 (2023).
143. Thornalley, D. J. R., Elderfield, H. & McCave, I. N. Holocene oscillations in temperature and salinity of the surface subpolar North Atlantic. *Nature* **457**, 711–714 (2009).
144. Lynch-Stieglitz, J. The Atlantic Meridional Overturning Circulation and abrupt climate change. *Annu. Rev. Mar. Sci.* **9**, 83–104 (2017).
145. Fan, Y., Liu, W., Zhang, P., Chen, R. & Li, L. North Atlantic Oscillation contributes to the subpolar North Atlantic cooling in the past century. *Clim. Dyn.* **61**, 5199–5215 (2023).
146. Ritz, S. P., Stocker, T. F., Grimalt, J. O., Menviel, L. & Timmermann, A. Estimated strength of the Atlantic overturning circulation during the last deglaciation. *Nat. Geosci.* **6**, 208–212 (2013).
147. Voelker, A. H. L. et al. Variations in mid-latitude North Atlantic surface water properties during the mid-Brunhes (MIS 9–14) and their implications for the thermohaline circulation. *Clim. Past* **6**, 531–552 (2010).
148. Stein, R., Hefter, J., Grützner, J., Voelker, A. & Naafs, B. D. A. Variability of surface water characteristics and Heinrich-like events in the Pleistocene midlatitude North Atlantic Ocean: biomarker and XRD records from IODP Site U1313 (MIS 16–9). *Paleoceanography* **24**, PA2203 (2009).

149. Ivanovic, R. F., Gregoire, L. J., Wickert, A. D., Valdes, P. J. & Burke, A. Collapse of the North American ice saddle 14,500 years ago caused widespread cooling and reduced ocean overturning circulation. *Geophys. Res. Lett.* **44**, 383–392 (2017).
150. Deaney, E. L., Barker, S. & van de Flierdt, T. Timing and nature of AMOC recovery across Termination 2 and magnitude of deglacial CO_2 change. *Nat. Commun.* **8**, 14595 (2017).
151. Martrat, B. et al. Four climate cycles of recurring deep and surface water destabilizations on the Iberian margin. *Science* **317**, 502–507 (2007).
152. Howe, J. N. W. et al. North Atlantic deep water production during the Last Glacial Maximum. *Nat. Commun.* **7**, 11765 (2016).
153. Voelker, A. H. L. & de Abreu, L. A review of abrupt climate change events in the northeastern Atlantic Ocean (Iberian Margin): latitudinal, longitudinal, and vertical gradients. in *Abrupt Climate Change: Mechanisms, Patterns, and Impacts* (eds Rashid, H., Polyak, L. & Mosley-Thompson, E.) 15–37 (American Geophysical Union, 2011).
154. Roberts, N. L., Piotrowski, A. M., McManus, J. F. & Keigwin, L. D. Synchronous deglacial overturning and water mass source changes. *Science* **327**, 75–78 (2010).
155. Levitus, S., Antonov, J. I., Boyer, T. P. & Stephens, C. Warming of the World Ocean. *Science* **287**, 2225–2229 (2000).
156. Zhu, C. et al. Enhanced ocean heat storage efficiency during the last deglaciation. *Sci. Adv.* **10**, eadp5156 (2024).
157. Veres, D. et al. The Antarctic ice core chronology (AICC2012): An optimized multi-parameter and multi-site dating approach for the last 120 thousand years. *Clim. Past* **9**, 1733–1748 (2013).

Acknowledgements

The authors thank Chun-Yuan Huang, Hsien-Chen Tsai, Wei-Yi Chien, Wen-Hui Sung, and Ho-Ya Su for help with laboratory work.

Author contributions

Conceptualisation, methodology, visualisation, data curation, and writing—original draft: H.-M.H. Software: H.-M.H., G.M., and J.S.S. Analysis and investigation: H.-M.H., G.M., T.R., Q.R., E.R., C.-J.H., X.J., M.F.S.G., L.T., J.S.S., B.C., and M.C. Resources: E.S., M.Z., V.M., P.V., and C.-C.S. Writing—review and editing: G.M., M.F.S.G., Q.R., E.R., T.R., C.P., and C.-C.S. Supervision and project administration: H.-M.H. and C.-C.S.

Funding

C.-C.S. acknowledges grants from the Taiwan National Science and Technology (114-2116-M-002-016-MY3; 113-2926-I-002-510-G), the Higher Education Sprout Project of the Ministry of Education (112L901001), and National Taiwan University (114L890102). G.M. acknowledges support from the Ministerio de Ciencia e Innovación, Spain (PID2019-109653RB-I00, TRIOPACC; CNS2023-145305, NOVAMOON). L.T. acknowledges funding from the National Natural Science Foundation of China (NSFC, 42325705), the Chinese Academy of Sciences (xbzgzdsys-202217), and Science and Technology Innovation Project of Laoshan Laboratory (No. LSKJ202203300). T.R. acknowledges funding from Portuguese national funds from FCT - Foundation for Science and Technology through projects Hydroshift (PTDC/CTA-CLI/4297/2021), WarmWorld (PTDC/CTA-GEO/29897/2017), contracts UID/04326/2025, UID/PRR/04326/2025, and LA/P/0101/2020 (DOI:10.54499/LA/P/0101/2020). M.F.S.G. thanks the funding from IODP France and the French project ANR NEANDROOTS. J.S.S. thanks the funding from the Academy of Finland (projects 310649 and 331426). C.P. thanks the funding from the NSFC (42472244).

Competing interests

The authors declare no competing interests.

Additional information

Supplementary information The online version contains supplementary material available at https://doi.org/10.1038/s41467-026-73733-6.

Correspondence and requests for materials should be addressed to Hsun-Ming Hu, Gianluca Marino or Chuan-Chou Shen.

Peer review information *Nature Communications* thanks the anonymous reviewers for their contribution to the peer review of this work. A peer review file is available.

Reprints and permissions information is available at http://www.nature.com/reprints

Publisher's note Springer Nature remains neutral with regard to jurisdictional claims in published maps and institutional affiliations.